

EVALUATION OF MICROSTRUCTURE RESPONSE UNDER VARIOUS LOADING AND
BOUNDARY

CONDITIONS TO AID IN THE ESTABLISHMENT OF A THRESHOLD CRITERION
FOR MILD TRAUMATIC BRAIN INJURY

BY

WILLIAM MATTHEW TAYLOR

W. STEVE SHEPARD, COMMITTEE CHAIR

BETH A. TODD

KEITH A. WILLIAMS

MARK E. BARKEY

A THESIS

Submitted in partial fulfillment of the requirements
for the degree of Master of Science
in the Department of Mechanical Engineering
in the Graduate School of
The University of Alabama

TUSCALOOSA, ALABAMA

2011

Copyright William Matthew Taylor 2011
ALL RIGHTS RESERVED

ABSTRACT

In previous research studies, the geometric and elastic properties for a critical component of axon health, the microtubule (MT), have been determined using lateral indentation with the tip of an atomic force microscope (AFM). Although the response due to the indentations caused by the AFM was observed to be linear for most of the tests, forces greater than 300pN would result in a permanent irreversible collapse of the MT's structure. While the intent of those researchers was not to evaluate microtubule strength properties, that load can be used as a starting point to evaluate internal stress failure criterion for such structures. To that end, the current research is investigating MT strength by replicating the loading and boundary conditions in a finite element model. This work is an extension of previous work aimed at using this 300 pN point load to develop failure criteria for MTs under more realistic loading conditions. In the present work, modeling has been used to correlate the AFM point load response with the more realistic distributed loading conditions that would result during a brain injury event. Furthermore, the impact of nearby MTs on the stresses that occur under similar loading conditions has also been examined. Correspondingly, models that include dynamic wave propagation through the microtubule were also studied. These results were used to analytically examine different loading conditions in order to equate various scenarios so that the determination of a stress threshold related to MT structural failure could more easily be examined in later work. The failure criterion determined in both cases would aid in evaluating brain injury studies that involve pressure wave propagation in whole-head finite element models, even when such models represent the white matter using homogeneous properties.

DEDICATION

This thesis is dedicated to all the friends and faculty that took time out of their day to help me and answer my questions.

ACKNOWLEDGEMENTS

I would like to thank my chairman of this thesis, W. Steve Shepard, who allowed me to have this opportunity to conduct this research. Also, for always be willing to answer my questions and give me advice. I would also like to thank the other committee members, Beth Todd, Keith Williams, and Mark Barkey for their time and their inputs.

CONTENTS

ABSTRACT	ii
DEDICATION	iii
ACKNOWLEDGEMENTS	iv
LIST OF TABLES	vii
LIST OF FIGURES	viii
1. CHAPTER	1
a. BACKGROUND.....	1
b. MICROTUBULE GEOMETRY AND PROPERTIES	7
c. RESEARCH OBJECTIVES	7
d. APPROACH AND THESIS LAYOUT.....	9
2. CHAPTER	11
a. FINITE ELEMENT MODELS	11
b. MODEL PARAMETERS.....	12
c. POINT LOAD (PL) MODEL	12
d. POINT LOAD WITH PLATE (PLP) MODEL	13
e. RIGID PLATE (RP) MODEL	14
f. ATOMIC FORCE MICROSCOPY SINGLE ELEMENT (AFMSE) MODEL	16
g. ATOMIC FORCE MICROSCOPY FULL (AFMF) MODEL	17
h. COMPOSITE SINGLE ELEMENT (CSE) MODEL.....	19
i. LOADING SCENARIOS	24

j. SUMMARY.....	24
3. CHAPTER	25
a. SIMULATION RESULTS.....	25
b. <i>IN VITRO</i> STATIC STUDIES.....	25
c. <i>IN VIVO</i> STATIC STUDIES	39
d. <i>IN VIVO</i> TRANSIENT STUDIES.....	45
e. SUMMARY	49
4. CHAPTER	50
a. CONCLUSION.....	50
b. FUTURE RESEARCH.....	51
5. REFERENCES	52
6. APPENDIX.....	54

LIST OF TABLES

1. Material properties used in models	12
2. Von Mises stress as point load spacing varies at 90°	30
3. Von Mises stress as point load spacing varies at 45°	31
4. Loads needed to maintain a constant Von Mises stress	31
5. Natural frequencies of <i>in vitro</i> and <i>in vivo</i> MT cross section	45
6. Transient point loads	48

LIST OF FIGURES

1. The Axon	3
2. Microtubule assembly, organization and dynamics in axons and dendrites	5
3. Illustration of AFM experiments	6
4. Microtubule that has been permanently deformed by AFM scanning load	6
5. Point Load (PL) model with 300 pN static radial point load	13
6. Point Load with Plate (PLP) model with equally spaced static radial point loads	14
7. Rigid Plate (RP) model with uniform 0.238 MPa pressure	15
8. Atomic Force Microscopy Single-element (AFMSE) model with uniform pressure	17
9. Atomic Force Microscopy Full (AFMF) model with uniform 0.238 MPa pressure	18
10. Composite Single Element (CSE) model with uniform 3.75 MPa pressure	20
11. Modeled MT array showing spacing between microtubules and boundary.	21
12. Applied pressure loading for the <i>in vivo</i> transient CSE model	22
13. Illustration of Transient Point loads by case	23
14. Y-direction stress distribution of PL model	26
15. Tangential stress distribution of PL model	27
16. Radial stress distribution of PL model	28
17. Von Mises stress distribution of the PLP model	29
18. Illustration of locations of stress evaluation	30
19. Y-direction stress distribution of RP model	32
20. Tangential stress distribution of RP model	34

21. Y-direction stress distribution of the AFMSE model with 3.75 MPa load.....	35
22. Y-direction stress distribution of the AFMSE model with 0.148 MPa load	36
23. Tangential stress distribution of the AFMSF model	37
24. Y-direction stress distribution of the AFMF model	38
25. Tangential stress distribution of the AFMF model	39
26. Impact of horizontal spacing on maximum von Mises stresses in adjacent MTs	41
27. Impact of vertical spacing on maximum von Mises stresses	42
28. Y-directions stress distribution of the CSE model	43
29. Tangential stress distribution of the CSE model	44
30. Tangential stress distribution of the transient CSE model	47

CHAPTER 1

BACKGROUND

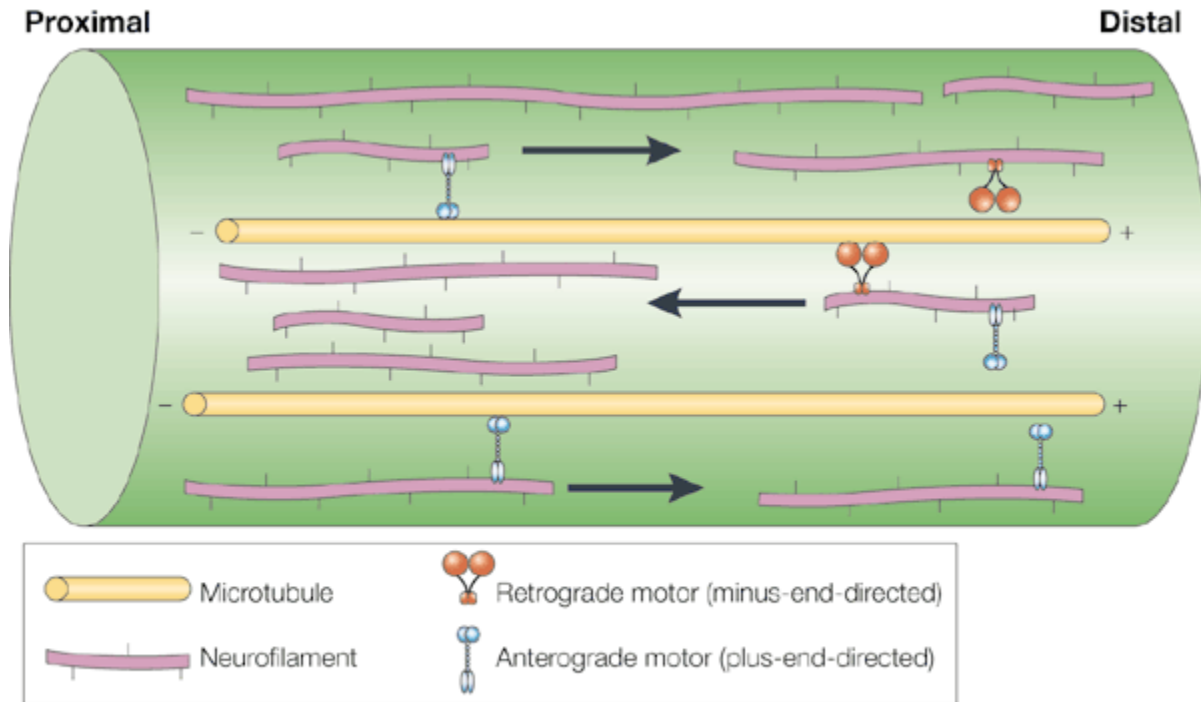
According to the Centers for Disease Control, 1.4 million civilians each year suffer from various types of traumatic brain injury. Of those 1.4 million, approximately 235,000 are hospitalized, and approximately 50,000 die as a result of those injuries (1). While the above figures apply to civilians, in the past 4 years the military has seen a 400% increase in the usage of improvise explosive devices (IED) in Afghanistan and a 700% increase in the numbers of injured soldiers (2). Injuries that result from blasts seen in combat are the leading cause of traumatic brain injury (TBI) in military personnel (4). In addition to apparent psychological issues, the consequences of TBI that can be visualized with modern medical devices include contusions and extra-axial hemorrhages. Yet, the more negative results of TBI occur at the microscopic level, which is referred to as diffuse axonal injury (DAI) (3, 16). Since 2000, there have been over 175,000 diagnosed soldiers. Of those soldiers, 130,000 were diagnosed with mild traumatic brain injury (mTBI) (4). The military has obvious concerns because IED shock waves induce closed-head injury, often in the form of this mTBI. Unlike the observable physical effects associated with TBI, the symptoms associated with mTBI are generally more inexplicit and can include delayed effects like memory deficits, impaired speech, difficulties with decision making, and insomnia (5). Because of the difficulty associated with diagnosing and treating mTBI, there is a need to develop new methods for understanding, diagnosing, and treating mild traumatic brain injury. To that end, the purpose of the work described here is to help understand the physical causes and mechanical loading thresholds associated with mTBI. More specifically,

this study involves utilizing a finite element method to model the mechanics of brain trauma at the microstructure level and analyze the response under severe loading conditions.

In recent years, there has been a growing wealth of research related to brain injury modeling. The goal of these works has been to accurately model the brain in order to evaluate and understand injuries that occur under different loading scenarios. One of the primary brain mechanical modeling approaches has been through the use of whole-head models, like the Wayne State Brain Injury Model, the University of New Mexico Head Model, and the Human Head Finite Element Model. These whole-head models are complex and encompass many of the structural components within the head (6, 17, 18). In these types of models, different mechanical loading scenarios, such as accelerations and impulses, are imposed on the head and various response parameters, like strains, stresses, and strain-rates, are evaluated. The ability to solve this type of finite element model relies heavily on the fact that the material properties of the brain are treated as homogenous. It is clearly not feasible to model the microstructures that makeup materials such as the brain white matter. Recall, however, that is the unobservable injury at the microscopic level that is believed to be the primary cause of mTBI (3). As a result of the need to use homogeneous material properties, the results of these simulations can therefore be inconclusive from the perspective of understanding the underlying injury mechanisms. The inability to understand the underlying mechanisms that produce injury has hindered the determination of specific brain injury thresholds, such as given accelerations or blast pressures.

As noted above, studies have shown that the more severe consequences of mTBI occur at the microscopic level. Again this type of damage is referred to as diffuse axonal injury (3). The axon, which is responsible for the transmission of information throughout the brain, is comprised

of many microscopic components as shown in Figure 1. Of these components, axons



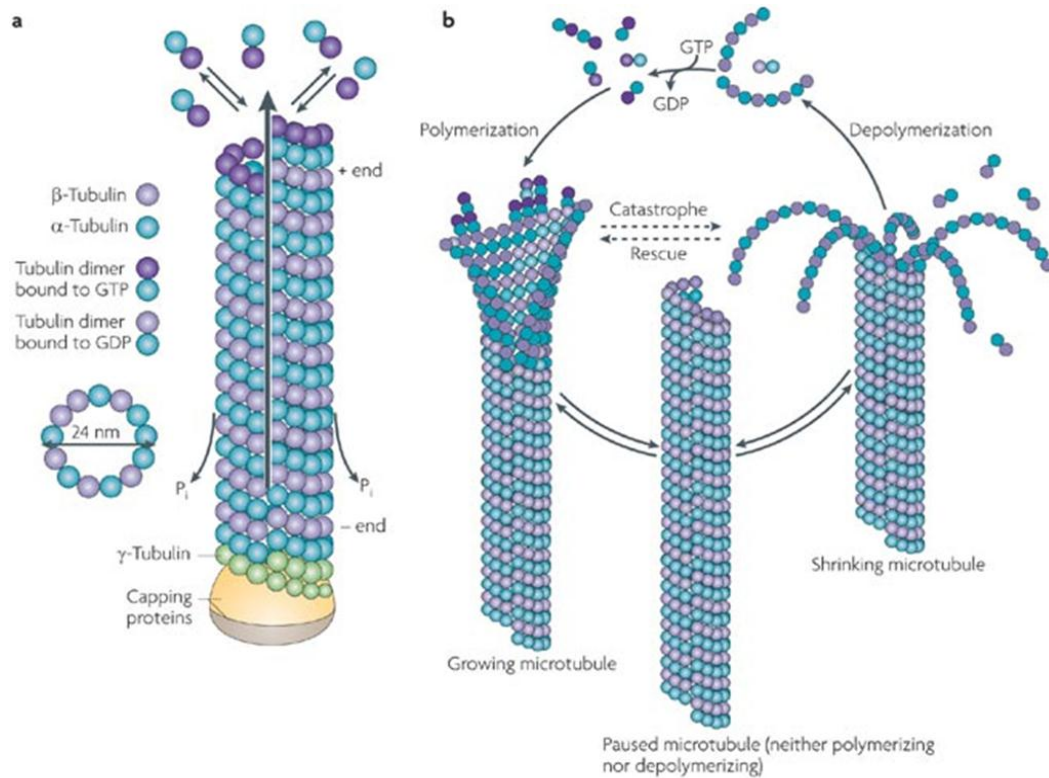
Nature Reviews | Molecular Cell Biology

Figure 1. The Axon (20).

get most of their structural support characteristics from microtubules and neurofilaments (7). Microtubules, hollow nanoscale components, provide important structural support and transport pathways that aid in the axons ability to function (8). In that, motor proteins walk along the microtubules to conduct intracellular transport of nutrients within the cell. These nutrients that are transported include a variety of organelles and vesicular cargoes (21). The impact of mechanical loading on these microscopic structures has not been assessed in detail due to the need to use homogeneous properties in the whole-head models described earlier. Again, it is not practical from the computational perspective in these whole-head models to model these structures on the nanometer scale. While there have been some studies involving measurement of the global properties of groups of these microstructures, little research aimed at examining

their mechanical response in detail as a single structure has been conducted. Two notable studies are the works of de Pablo *et. al* (11) and Schaap *et. al.* (12), which are discussed in more detail below. Since the health of axons is known to depend on these microstructures, the goal of the work described here is to continue the examination of brain injury modeling, but from a more microscopic perspective. To that end, the work cited above is used as a starting place in order to examine mTBI via modeling, but from the perspective of axonal microtubule (MT) response and failure.

Of the rod-like structures mentioned above, microtubules (MTs) are the most rigid (9). In Figure (2), the molecular assembly and disassembly of these microtubules can be seen. Axons contain both stable and unstable MTs, which are dynamically responsible in the growth and maintenance of the axon. It was shown in the works of Baas *et. al*, that through the use of drugs, labile and stable microtubules dynamic behavior can be effected. When labile MTs were depolymerized by the use of drugs, the MTs would begin repolymerizing. For stable MTs, though, this important repolymerization did not occur after treatment with these drugs (24). This observation can be extended to consider the long-term effects of pressure wave loading that causes stable microtubules to be damaged or depolymerize, which would inhibit the transportation of nutrients along them via motor proteins. As a result, the damage of stable MTs seem particularly relevant to the brain damage issue.



Nature Reviews | Neuroscience

Figure 2. Microtubule assembly, organization and dynamics in axons and dendrites (23). In one of the works mentioned above, the elastic properties of MTs were measured using atomic force microscopy (AFM) by subjecting a single MT sample to radial loads and observing the MT's reaction (11). From these experiments, it was observed that when a radial scanning load exceeding 300 pN was applied to a microtubule, as denoted by F_{\max} in Figure (3), irreversible damage occurred as shown by the damaged region in Figure (4). Yet, when a scanning load less than 300 pN was applied, the MT always returned to its original shape, also seen in Figure (4). This force, albeit approximate, provides a starting point to evaluate the loading and failure mechanisms within this brain microstructure via a numerical study.

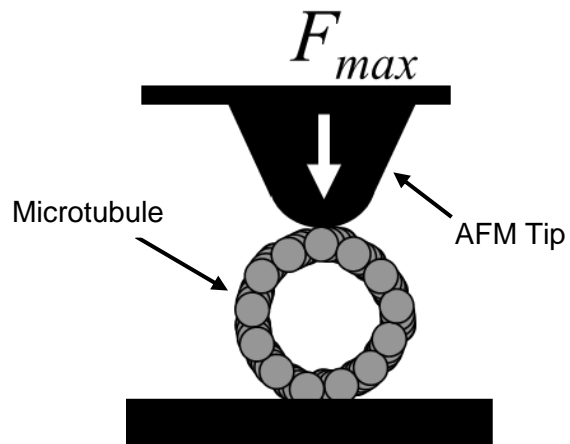


Figure 3. Illustration of AFM experiments like those done in Pablo et. al.(12).

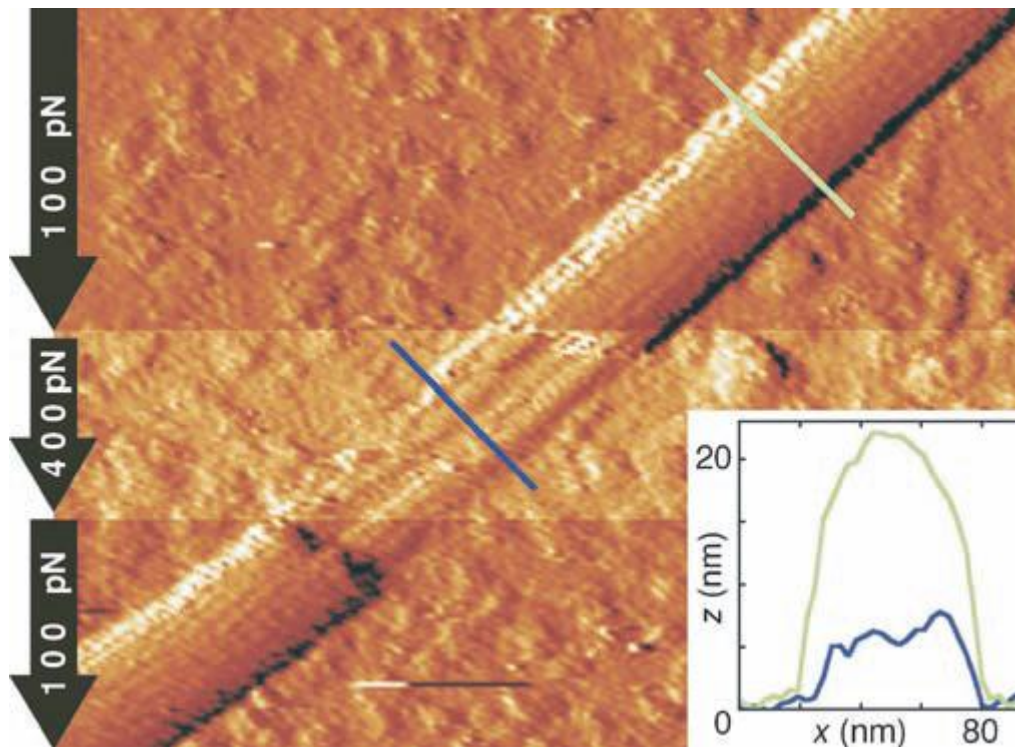


Figure 4. Microtubule that has been permanently deformed by AFM scanning load (23).

MICROTUBULE GEOMETRY AND PROPERTIES

In order to perform an analytical study to determine the loading and response characteristics associated with mechanical failure, an appropriate geometric representation of the MT is needed. In a recent work by Schaap *et. al.* (12), equivalent elastic mechanical properties for MTs were determined. From that work, an effective simplified geometric representation of the MT was determined by using finite element methods. This more simplified geometry is used here, where the microtubule is to be modeled as a simple hollow tube with an outer diameter of 19.88 nm and an inner diameter of 16.8 nm. By using all-atom simulation systems and continuum elastic modeling, Sept and MacKintosh were able to calculate a Young's modulus of 2.2 GPa for a MT. This attained Young's modulus is based on an assumed Poisson's ratio of 0.3, and in the present study the same value is used (10). From the work of Jiang and Zhang, the Young's modulus of cytoplasm is found to range for 0.1 Pa to 1000 Pa (26). In this study, the latter value of 1 kPa is used along with an assumed Poisson's ratio of 0.499.

RESEARCH OBJECTIVES

By utilizing the results of the works mentioned above, the specific goal of the research described here is to correlate loading in the previously conducted AFM experiments (11, 12), as illustrated in Figure (3), via modeling to determine an equivalent response characteristic associated with axonal MT failure due to the specific loads applied to the MT. While the AFM loads that resulted in failure would more appropriately be represented as a point load, such loading would not necessarily be equivalent to that experienced during a brain injury event. During a brain injury event, the loading would more appropriately be described as distributed and transient. As a result, it is important to examine correlation in the response on the axonal MT when subjected to the different types of loading. Once these correlations are obtained,

future experiments can be conducted in a more meaningful manner to actually measure the mechanical pressure loading threshold. The ultimate benefit of this work would be to provide specific MT failure characteristics and enable those modelers using a whole-head approach the ability to better predict loading scenarios that lead to injury while continuing with the use of homogeneous material properties.

As noted above, this work describes a study in which previously conducted AFM experiments (11, 12) involving microtubule mechanical failure are examined using finite element methods. This research is an extension of previous work done by Zhang and Shepard, which established much of the foundations used for the present study (15). One important issue that must be addressed in the present study involves a reasonable description of the complex loading provided by the AFM tip as well as the boundary conditions. Because of the complex nature of the AFM loading, several different models are utilized to help gain a better understanding of the important characteristics of that loading. Note that this study examines the static loading considerations from those AFM studies and dynamic characteristics of the *in vivo* scenario possible during an injury event. Not only will this *in vitro* AFM loading condition be modeled, but the *in vivo* conditions that a MT would experience are also examined. Such a study involves further complications in attempting to correlate an AFM failure load with an analogous distributed load that would be experienced *in vivo*. To accomplish this correlation, various models are used in an attempt to equate stresses produced by the point loading of AFM with stresses produced by a pressure loading that would be experienced *in vivo* during a blast event. To help with this correlation, both Cartesian and cylindrical coordinates are used in studying the response characteristics. Besides the type of loading, there are several other important considerations that must also be considered in the *in vivo* portion of the study. In that portion of

the study, the impact of nearby MTs on the response characteristics is examined. Because axonal MTs are collinear, the effect of other nearby structures on the resulting response may be an important characteristic. As noted earlier, microtubules also provide a pathway for motor proteins to power cellular motility. Along with providing necessary nutrients to the cell, motor proteins can transport MTs within the cytoskeleton. The height of motor proteins that would correspond to a MT spacing, like in Figure (1), is approximately 8 nm (19). Because these motor proteins may in fact connect two MTs, the impact of this small spacing on the resulting stresses during an *in vivo* loading simulation should be considered.

APPROACH AND THESIS LAYOUT

In trying to understand the loading characteristics that were present in the aforementioned AFM studies, a set of finite element static loading simulations will first be done. In modeling the AFM experiment, various modeling and loading approaches will be used. Those loading approaches will consider different load types, such as point loads, as well as different support boundary conditions. As noted above, the objective will be to gain a better understanding of the axonal MT response characteristics. Once the loading and resulting stress distributions are understood, transient loading conditions will be examined. This transient loading will depict a more accurate loading scenario for brain injury and allow for the investigation of pressure thresholds. Much work has been done to evaluate wave propagation in the brain, but not on a microscopic level. This study will allow for a more accurate correlation of pressure blasts to stress response of microtubules. Along with the resulting stresses seen in the transient loading simulations, the subsequent natural frequencies will be calculated. By having these natural frequencies, it will be possible to evaluate the relevance of the AFM and other

static loading conditions in estimating and comparing stresses in a MT subjected to loading of a transient nature.

The following chapter reviews the structure of the MT along with other topics relevant to the finite element models used in the simulations. As will be seen, each of these models differs primarily in the manner in which the loading is applied. Once those topics are addressed, results from the simulations are provided in a subsequent chapter along with some general discussion of the observations made.

CHAPTER 2

FINITE ELEMENT MODELS

In this chapter, the Finite Element models that were developed and considered are discussed. As noted above, the objective is to gain an understanding of a correlation between the AFM loading and transient brain injury loading scenarios for the relevant response characteristics. To that end, various Finite Element models were used. These models, which will be discussed in detail below, include: the point load (PL), point load with plate (PLP), rigid press (RP), atomic force microscopy single element (AFMSE), atomic force microscopy full (AFMF), and composite single element (CSE) models. All of these models are considered *in vitro* except for the CSE model, which attempts to represent the MT *in vivo*. In these models, 20-node brick elements are used to mesh the various materials. All material properties are assumed to be linear isotropic. Although biological material properties tend to vary with frequency, it was assumed that they remain constant in this study. Nonlinear or frequency-dependent properties will be considered in future research. Furthermore, all of the listed models were meshed such that the resulting stresses did approach a converging result (see appendix for example) even though it may not be referenced directly in the results section. Recall that the objective in using various models is to gain a more fundamental understanding of the impact of various loading scenarios on the possible developing stresses as well as correlate this analytical approach to the experimental AFM study. It is not believed that one of these models, as an

individual model, necessarily provides a more accurate assessment of the MT response. As a result, one model should not be deemed better than the others.

MODEL PARAMETERS

Each of the subsequent models were meshed using ANSYS APDL with a 20-node brick element, SOLID95, which has a compatible displacement shape and is well suited to model curved boundaries. This element has three degrees of freedom per node, which implies translations in the nodal x, y, and z directions. This element was chosen because it can have any spatial orientation, along with the capability to have large deflection and strain. Depending on the structure to be modeled, each brick element is coupled with material properties of steel, MTs, or cytoplasm, which are all assumed to be linear isotropic. Though the material properties in microtubules and cytoplasm may depend on the direction loading, which is indicative of anisotropic behavior, these differences are not considered in this study. The isotropic properties used in the various models are listed below in Table (1). With this general information, it is now possible to discuss each specific model.

Table 1. Model material properties used.

Material	Young's Modulus (Pa)	Poisson's Ratio	Density (kg/m ³)
Steel	2.07E+11	0.292	7800
Microtubule (MT)	2.20E+09	0.3	1470
Cytoplasm	1.00E+03	0.499	1040

POINT LOAD (PL) MODEL

In the PL model shown in Figure (5), a microtubule of a finite length of 100 nm is subjected to a point loading of 300 pN in the negative vertical axis located at the MT center top while a pinned constraint is applied to a line of nodes along the length of the bottom of the MT.

The geometry below is meshed with 1600 20-node brick elements. This model represents the AFM experiments with the assumption that the AFM produces a concentrated point load and the supporting base can be represented by a pinned connection. Unless specifically stated otherwise, it can be assumed that all the loads listed are static. Simulation results from this and all subsequent models will be discussed in the next chapter.

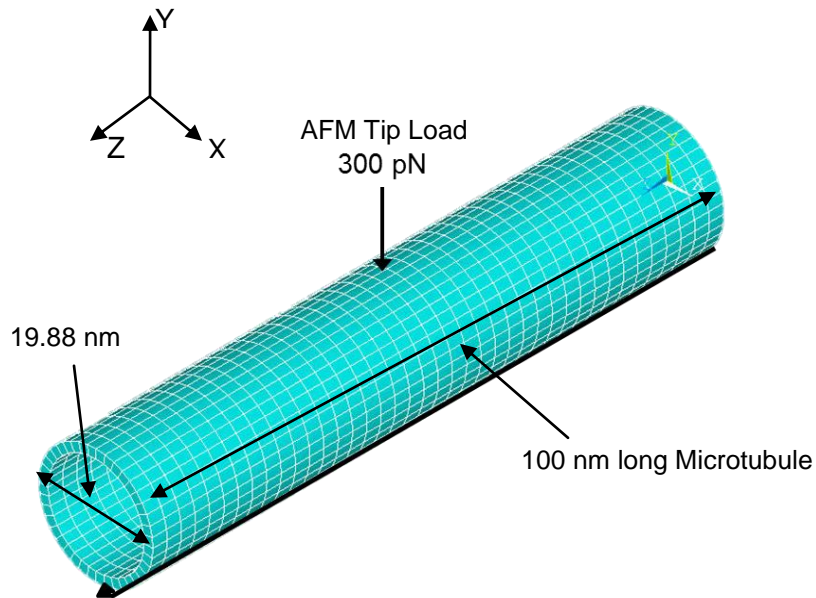


Figure 5. Point Load (PL) model with 300 pN static radial point load.

POINT LOAD WITH PLATE (PLP) MODEL

In the PL model discussed above, just one point load was considered. However in the Point Load with Plate (PLP) Model, Figure (6), multiple point loads are applied to investigate point load spacing and the resulting stress distribution. This model also will help determine what spacing between the loads would best represent distributed loading. Such information would be quite useful in future experimental studies, such as those that could utilize various methods to impose loading in a more controlled manner. With a better understanding of the loading spacing

that adequately mimics a distributed loading, it may be possible to perform more realistic loading during *in vitro* experiments.

This model is comprised of a 100 nm long tube resting on a rigid steel plate. The plate is constrained at its base in all directions to represent a rigid foundation. In this simulation, the microtubule is meshed with 2304 20-node brick elements and the steel plate has 384 20-node brick elements. The tube will be subjected to point loads of identical magnitudes along the top surface, which will all be in the negative vertical axis. Nevertheless, these loads will be scaled to compare load magnitude to spacing in order to maintain a constant stress.

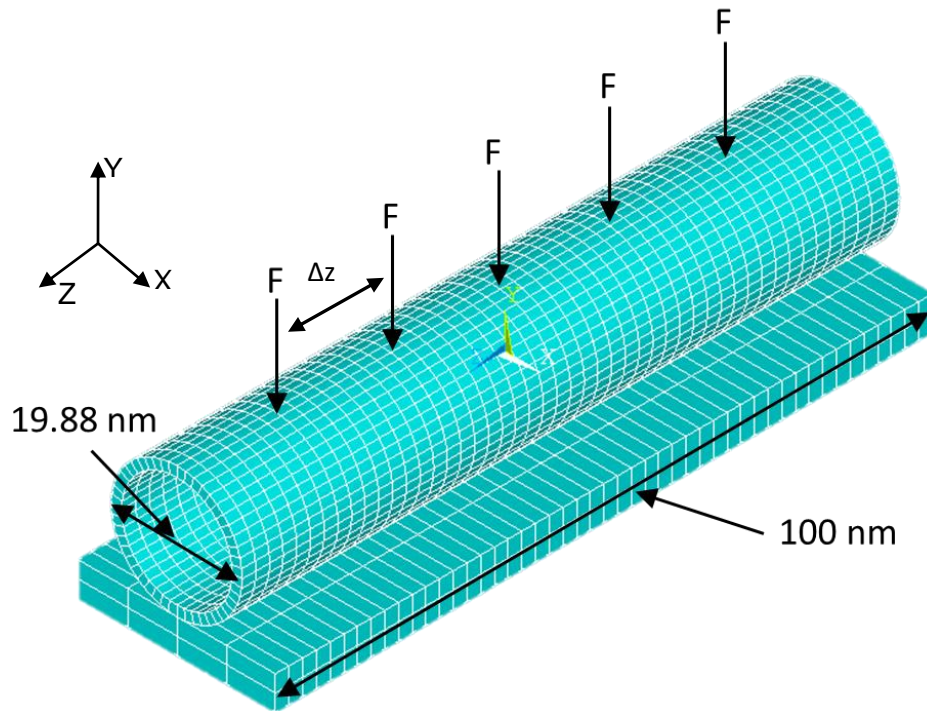


Figure 6. Point Load with Plate (PLP) model with equally spaced static radial point loads.

RIGID PLATE (RP) MODEL

To eliminate any stress concentrations produced from the point load applied and to further understand the impact of the loading on the stresses within the MT in the model described

above, the rigid plate (RP) model illustrated in Figure (7) allows for a potentially more accurate description of the loading mechanics that arise in the microtubule during an AFM experiment, particularly since the AFM tip is large when compared to the dimensions of the MT diameter.

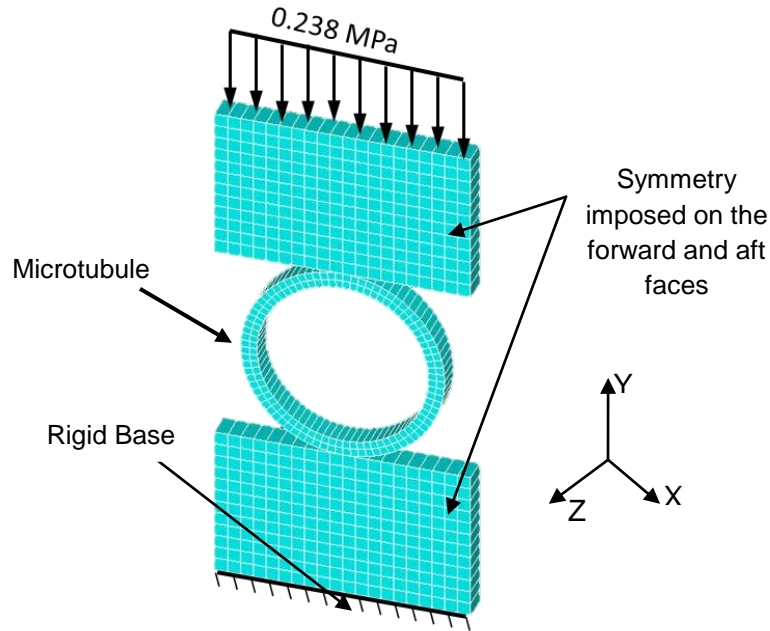


Figure 7. Rigid Plate (RP) model with uniform 0.238 MPa pressure.

Therefore, the mechanics in the RP model are based on the fact that the radius of the AFM tip, 20 nm, is treated as infinite when compared to the radius of the microtubule, 9.94 nm. To consider this, the tube in this model is loaded on the upper and lower surfaces by two steel plates. To represent an infinite MT, a 2 nm long model is constructed with z-direction symmetric boundary conditions on each xy face of the model, i.e. zero z displacement. In the RP model, the steel plates each are meshed with 240 20-node brick elements and the microtubule is meshed with 160 20-node brick elements. The nodes that are shared by the microtubule and the steel plates are merged to couple the two geometries. A load is initially calculated by distributing the 300 pN point load of the entire upper area of the top plate. This final load is derived by adjusting the pressure magnitude on the top plate until the stresses in the y-direction

match that of the PL model. This evenly distributed load ends up being 0.238 MPa. Furthermore, the base of the bottom plate is rigidly constrained in all directions to further represent the conditions of the AFM experiments. By using this approach, the impact of the tip loading of stresses in the other directions can more readily be assessed in the context of mimicking a more even loading condition.

ATOMIC FORCE MICROSCOPY SINGLE ELEMENT (AFMSE) MODEL

Even with the understanding provided by the above models, another model was created to better simulate the AFM tip loading geometry. To accomplish this, the upper plate in the PB model is refined to be more geometrically similar to an AFM tip, as shown in Figure (8). Because of the size of the AFM tip relative to the MT size, as noted above, localized loading of this nature may be similar to that produced by an infinitely long tip. As a result, a model that represents an infinitely long AFM tip with the same radius was examined through the Atomic Force Microscopy Single Element (AFMSE) model. This model consists of three component cross sections, the AFM tip, the MT, and a rigid base, all of which have a thickness of 2 nm. The AFM tip and base plate both are modeled as steel. The AFM tip with a radius of 20 nm is loaded with a distributed loading on the top surface. The base of the bottom steel plate is constrained rigidly in all directions, again to replicate the AFM experiments. The base plate geometry is meshed with 83 20-node brick elements. The AFM tip here is meshed with 3127 brick elements and the MT is meshed with 340 brick elements. The load on the AFM tip is also scaled until the stresses within the MT match that of the previous models. It should be noted that, as in the previous model, the axial faces have symmetric boundary conditions to represent the aforementioned infinitely long MT and tip. Furthermore, the condition is imposed so that the MT surface cannot penetrate the surface of the AMF tip or base.

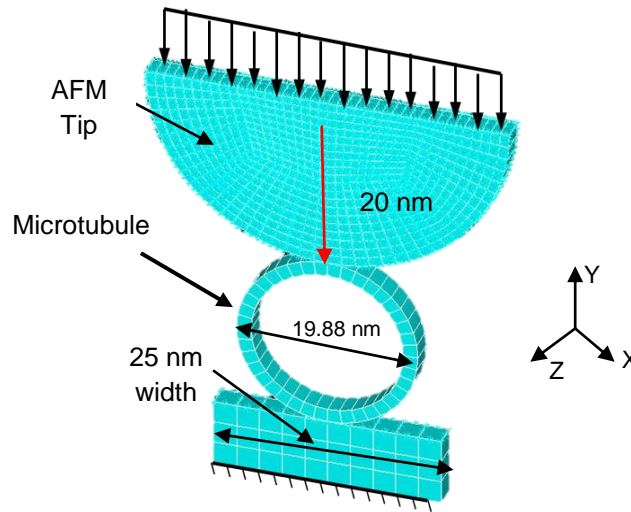


Figure 8. Atomic Force Microscopy Single-element (AFMSE) model with uniform pressure.

ATOMIC FORCE MICROSCOPY FULL (AFMF) MODEL

Further motivation to understand the scale of the AFM tip resulted in the development of a 3D model that includes an AFM tip geometry that is finite in two directions. This model is called the AFMF model as illustrated in Figure (9). In this model, the AFM tip is treated as a hemisphere (radius of 20 nm) in contact with a finite length hollow tube (100 nm). The tube is resting on a steel plate, which is pinned in all directions. All of the material properties used in the AFMF model were listed back in Table 1. The microtubule section here is meshed with 6871 20-node brick elements, while the AFM tip section is meshed with 967 20-node brick elements and the steel base is meshed with 469 20-node brick elements. As in the previous model, a distributed load is applied to the top surface of the AFM tip. The load here is based on the area of the top surface of the MT and the initial 300 pN load, which results in a load of 0.238 MPa. The AFM tip here is constrained only to move in the vertical direction. In the AFMF model, contact elements are used to control the interaction between the AFM tip and the microtubule.

The contact elements used here have 8 nodes and the associated target element has 8 nodes. The contact surface (MT) is bonded to the target surfaces (AFM tip and rigid base) for this simulation, and is assumed to be frictionless.

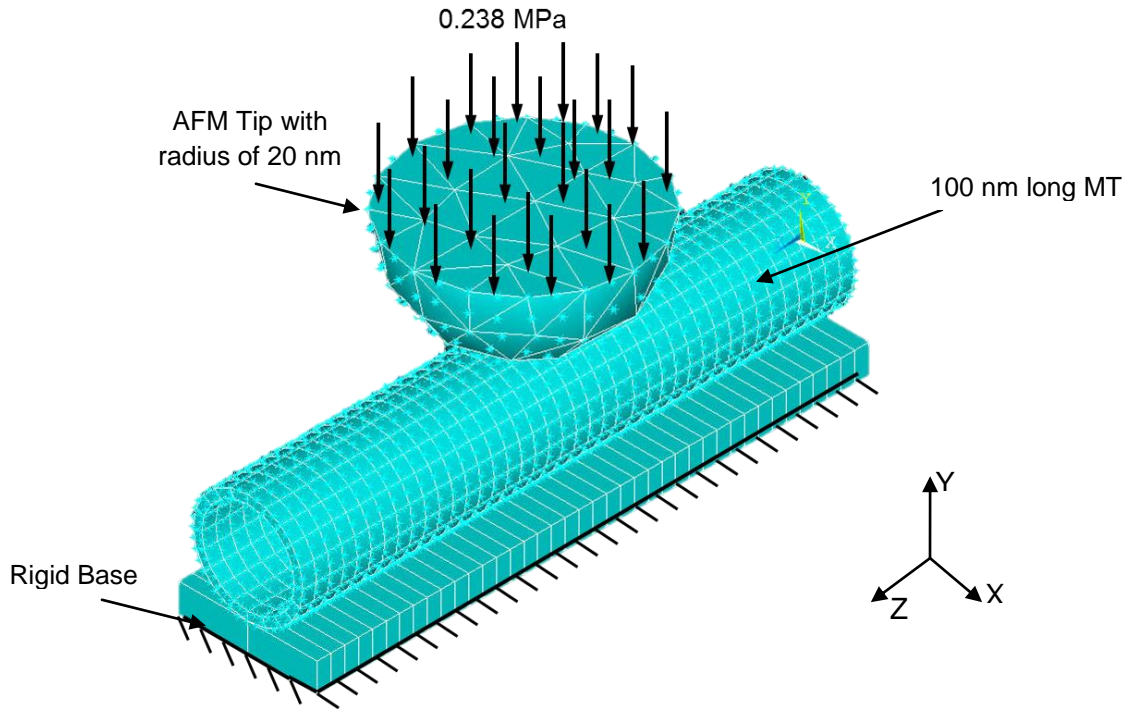


Figure 9. Atomic Force Microscopy Full (AFMF) model with uniform 0.238 MPa pressure.

One might at this point question the need for the previously mentioned models when the AFMF appears to better represent the actual geometry of the AFM experiment. By utilizing these different approaches, however, it is hoped that the important characteristics of the failure mechanics and the correlation between the loads and the stresses can be more readily identified. Accordingly, to relate the AFMF model to a more realistic distributed loading in mTBI, a correlation between the models may be useful. For example, it may be determined that the stress concentrations produced in some of the models may not be important when considering how a MT might actually be loaded in the AFM experiment being modeled. Furthermore, depending

on the boundary conditions used, the overall stresses in the tube might vary. This behavior also helps understand the importance of these characteristics, which will be noted in the results section below.

COMPOSITE SINGLE ELEMENT (CSE) MODEL

All of the models described thus far consider AFM loading of the microtubule from an *in vitro* perspective. Again, this is done to help correlate the important MT response characteristics with the failure observed in AFM experiments. In order to correlate the important response results to *in vivo* MT failure associated with mTBI, it is necessary to account for the effects of the cytoplasm that is known to surround and fill the MT in the axon. The Composite Single Element (CSE) model was created to examine this configuration. This model is considered to be *in vivo* because it is representing an infinite tube suspended in cytoplasm, as illustrated in Figure (10). As in previous models, symmetry is being imposed on the xy faces so that an infinitely long MT is being modeled in the z direction. In addition, the MT has been sliced vertically to impose symmetry along that face as well as along the opposite parallel face. The base of the model has a pinned constraint in all directions.

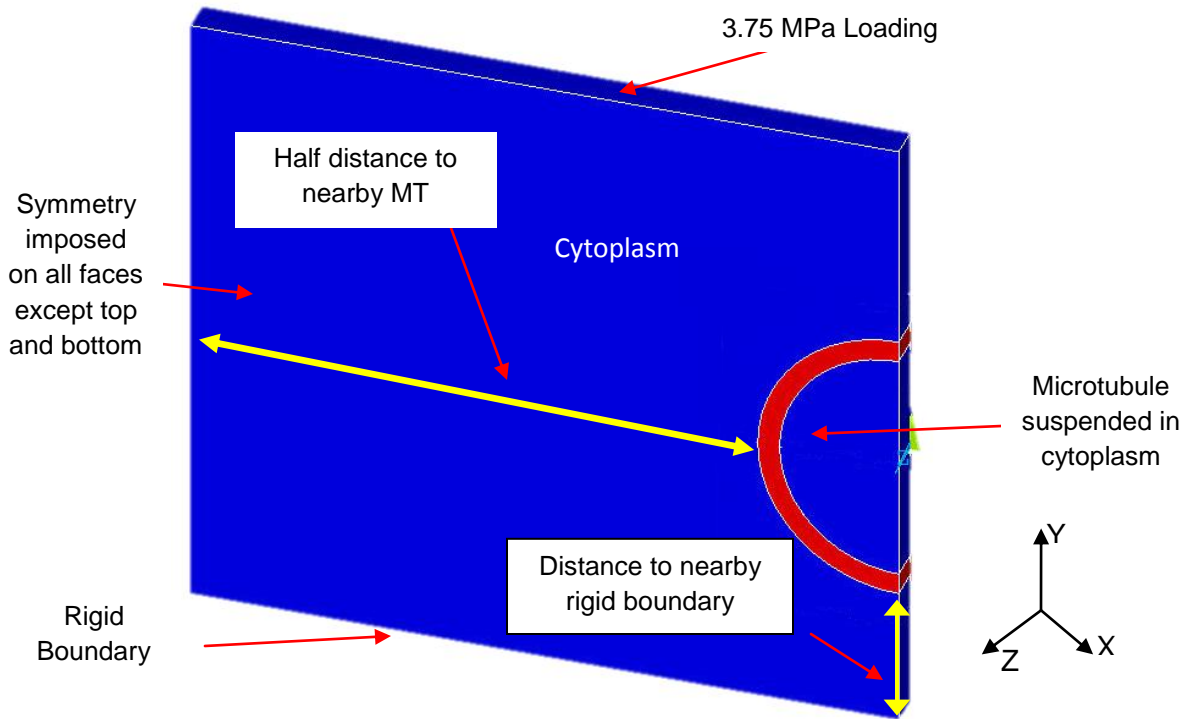


Figure 10. Composite Single Element (CSE) model with uniform 3.75 MPa pressure.

By using the above symmetric boundary conditions, the impact that neighboring MTs have on the MT loading and resulting stress distribution can be easily examined by adjusting the distance between the microtubule and the opposite cytoplasm boundary where symmetry is imposed (see figure). At this symmetry face, a mirror of the MT is provided such that an array of equally spaced MTs is actually being considered as illustrated in Figure (11). The impact of the nearby MTs may influence the resulting stresses in the MT and provide a lower or higher threshold for mTBI. As a result, it is important to understand how such spacing impacts the stresses. A simple representation of microtubule spacing can be seen in Figure (11). By varying the dimensions of the geometry in this relatively simple single-element width model, the impact of nearby MTs can be studied with greater ease.

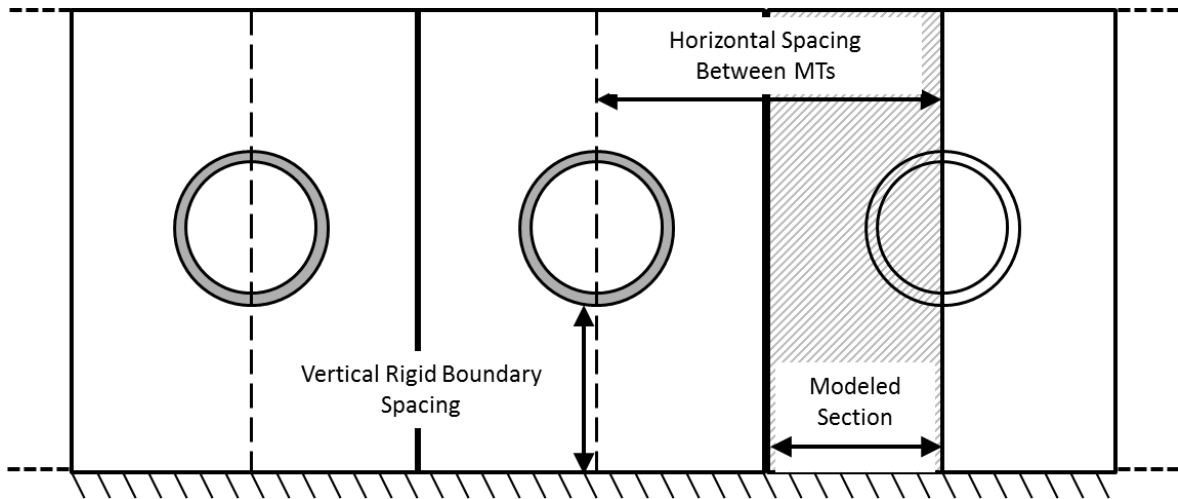


Figure 11. Modeled MT array showing spacing between microtubules and boundary.

The impact of nearby boundaries can also be examined in this model by adjusting the distance of the MT from the lower boundary, where a rigid boundary condition is imposed (see Figure 9). This study is useful in examining the impact of nearby rigid structures within the brain, like bone, on the MT response. Once the effects of these nearby structures are determined, this model will be modified accordingly and used to study the transient effects of the dynamic loading with point loads and pressures.

The applied transient pressure wave loading of the CSE model can be seen in Figure (12). Here two different loading scenarios are examined. One is a single step and the other is an impulse with a positive pulse that is twice the magnitude of the negative portion. It may be noted that the time range in Figure (12) is roughly 20 percent of the total time range over which the simulation occurs. Also, note that the transient nature of this loading is significantly faster than that of which would be experienced during a brain injury event, and that this loading is used to merely examine the wave propagation within the microtubule. For example, a typical blast pressure wave has a timescale on the order of 2 msec, while these waves are imposed over 80

picoseconds. The faster loading used here was done to introduce transient waves into the relatively stiff MTs.

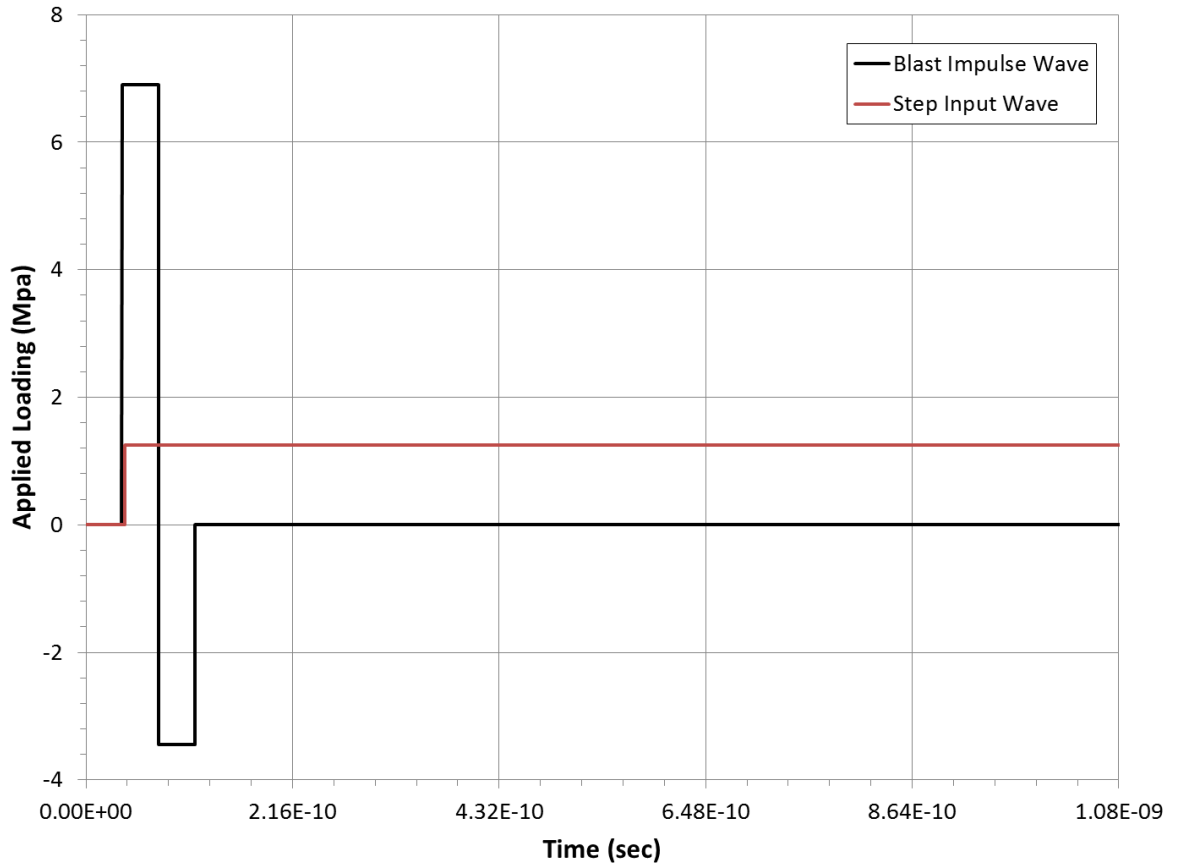


Figure 12. Applied pressure loading for the *in vivo* transient CSE model.

In addition, transient single point loads will be used to correlate the stresses seen to stresses observed in transient pressure loading cases. This will be done by placing point loads at different nodes along the radius of the MT, which can be seen in Figure (13). Please note that point loads in Figure (13), (A), (B), (C) all correspond to the different loading locations that are considered individually. Also note that the loads resulting from symmetry of the model are not shown in the figure.

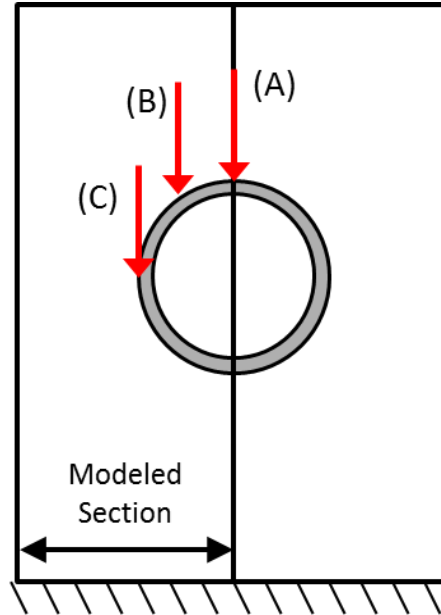


Figure 13. Illustration of transient point loads by case.

The results found will be used along with the static *in vivo* models described above to examine the impact of traveling transient pressure waves on the resulting stresses within the MTs. One goal of the study will be to determine a minimum pressure pulse that is believed to produce failure within the MT structure based on comparing the important resulting stresses with those found in the above studies. The more realistic objective, however, is to gain a better understanding of how the responses in the various loading scenarios correlate. With this information, it will be possible to determine cases that are believed to be more representative of actual brain loading conditions. Furthermore, the impact of the pressure magnitude and duration can be examined with the goal of understanding possible blast loadings that might produce mTBI.

LOADING SCENARIOS

In the models describe above, it is important to consider how the microtubule is to be loaded. As a result, the loading to be used in the aforementioned models will vary accordingly to the model. In the Point Load (PL) and Point Load with Plate (PLP) models, only static point loads are used. While in the Rigid Plate (RP), Atomic Force Microscopy Single Element (AFMSE), Atomic Force Microscopy Full (AFMF) models, static pressure loads are only studied. Finally, in the Composite Single Element (CSE) model, static and dynamic pressures and transient point loads are examined. That is, a transient step and impulse wave (Figure 12) is considered as well as transient point loads. While the purpose of this study is to correlate certain loading conditions to the stress distributions within the microtubule, no such scenario is deemed better.

SUMMARY

This chapter has presented a detailed overview of the finite element models that will be used in the course of the study. These models include different geometries and boundary conditions as well as different approaches to impose the loading. By using these models, it is hoped that the simulation results, to be discussed in the next chapter, can be used to better understand the resulting response characteristics within the context of mTBI.

CHAPTER 3

SIMULATION RESULTS

In this chapter, the associated response results for each of the simulations will be discussed. The PL model will be the starting point of the discussion and the other models will follow according to the order in which they were described in Chapter 2. This chapter also provides the effects of static loading versus transient loading. In addition a correlation of the AFM experiments will be made to a more specific loading scenario. Although not discussed in great detail, a simple comparison with an analytical model is also mentioned with additional details provided in the appendix.

IN VITRO STATIC STUDIES

As noted earlier, a model was first created to represent the AFM experiments under the assumption that the AFM produces a concentrated point load, (see Figure 5). From the analysis of the PL model, a high stress concentration around the point load is seen as expected in the resulting stresses shown in Figure (14). Though the mesh in the vicinity of the point load was

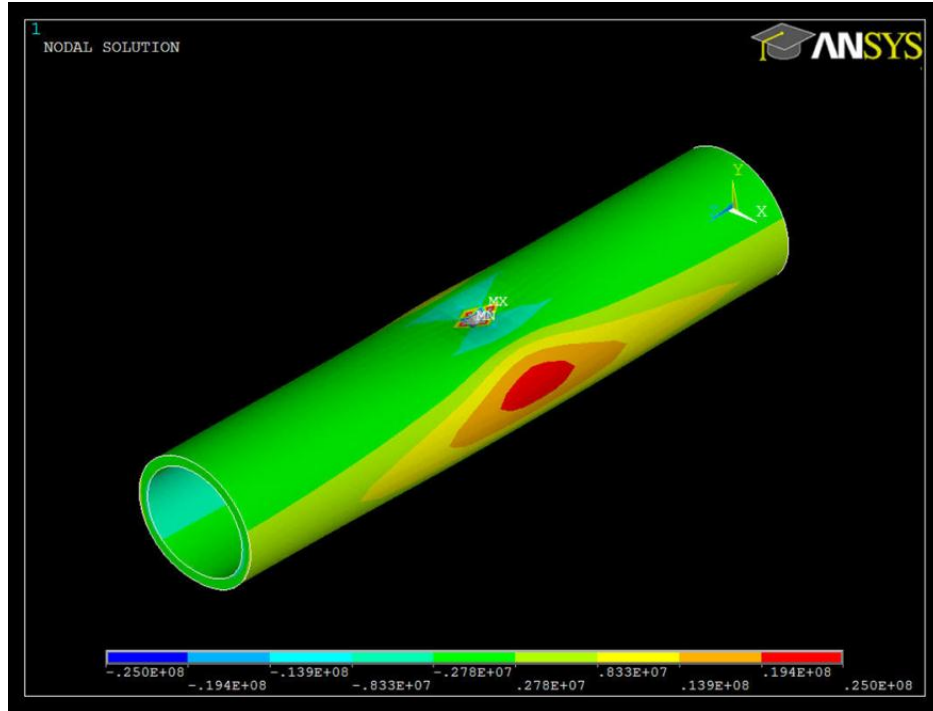


Figure 14. Y-direction stress distribution of PL model.

refined to ensure convergence. These maximum y-direction stresses, σ_y , located at the location of the point are 35 MPa and -272 MPa and will be ignored. From observation of the different stress plots, the stresses that occur in the y-direction have among the highest magnitudes. The next highest stresses appear on the outer and inner surface of the MT along the side. These y-stresses are located midway on the side of the tube. The values for these stresses are 22.5 MPa and -28.2 MPa respectively. Note that due to the presence of a bending stress and a superimposed axial stress, these extreme stress values are not symmetric. As with typical convention, a positive value denotes a tensional stress while a negative stress denotes compression. As expected, the stresses rapidly decrease as one moves down the MT axis from the point of the load application.

In terms of cylindrical coordinates, the loading produces a maximum tangential stress, σ_t , of 165 MPa and a minimum σ_t of -278 MPa at the location of the loading. The tangential stress distribution can be seen in Figure (15). In addition, the maximum radial stress, σ_r , is 37.4 MPa

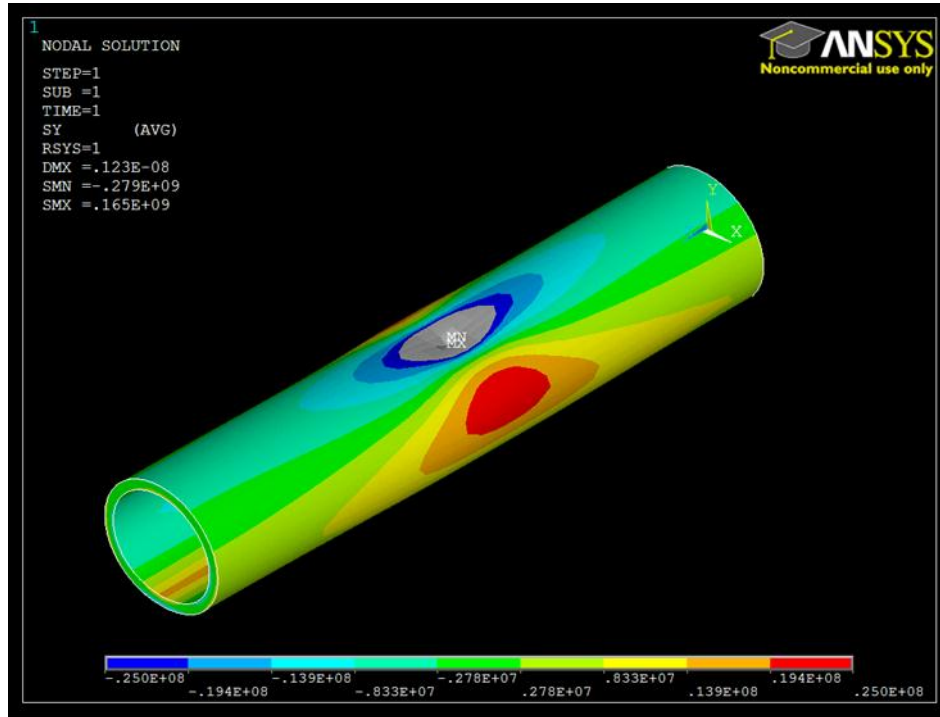


Figure 15. Tangential stress distribution of PL model.

and the minimum σ_r is -272 MPa. Also, the tangential stresses in the side walls of the MT are identical to the y-directions stresses, which is expected. The radial stresses can be seen if Figure (16). In this plot, the radial stresses have the greatest magnitudes around the location of the point load. However, as seen below, the stress at locations away from the point load are approximately zero. The zero radial stresses are as expected from such a long tube with no axial loading. Again, these high values are due to stress concentrations and are not necessarily deemed important.



Figure 16. Radial stress distribution of PL model.

The Point Load with Plate (PLP, Figure 6) model was used to understand more of the loading mechanics of microtubules than to establish stress thresholds. In trying to validate the numerical values established in the PLP model, an analytical comparison of maximum bending stress is made using a circular ring under a concentrated load approximation. From the numerical results, the maximum bending stress was found to be 147.9 MPa. When compared to the analytical approximation, which was calculated to be 151.3 MPa, there was an approximate 2.2 percent difference in the two. The full procedure used can be seen in the appendix.

With the PLP model, only the Von Mises stresses that occur on the outer surface of the MT, midway down vertically are considered. The model is initially subjected to 23 point loads along the top, which are spaced 4.2 nm apart. These forces each have a magnitude of 300 pN and are applied in the negative vertical direction. This scenario is clearly representative of

uniform distributed loading, resulting in a Von Mises stress of 250 MPa located at the outer side of the MT, which can be seen in Figure (17). Since the stresses away from the end are clearly similar to the case of distributed loading, this case will be taken as a reference case, to examine the impact of increasing the load spacing, which will be discussed next.

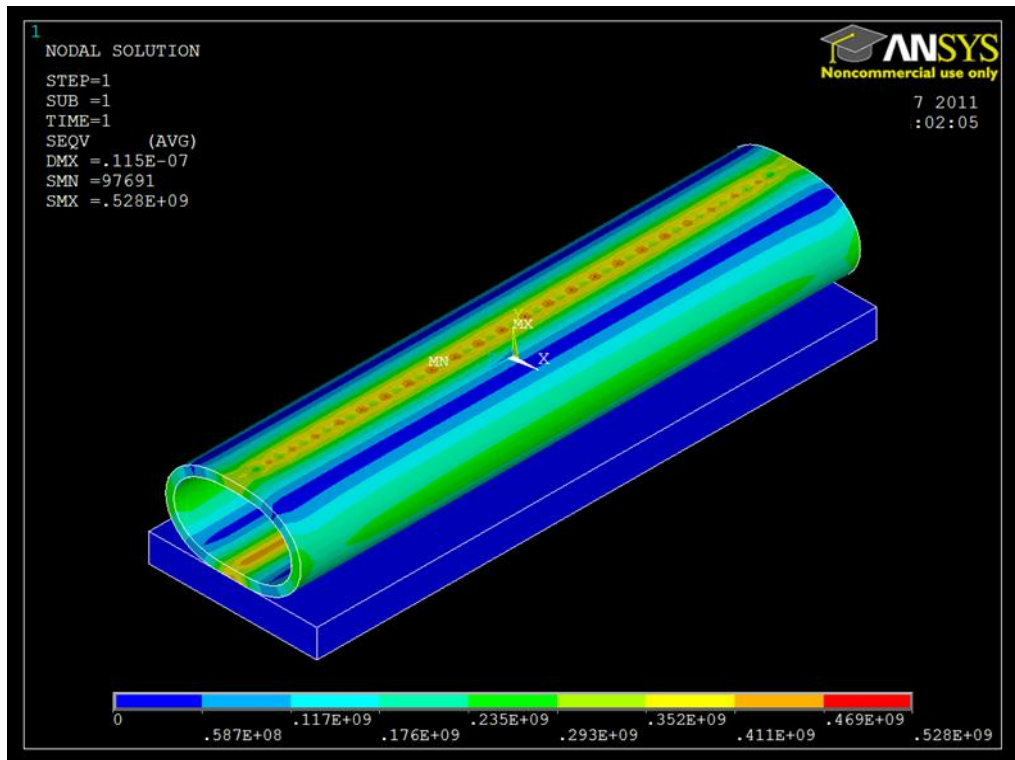


Figure 17. Von Mises stress distribution of the PLP model.

From this point the spacing is doubled in each successive simulation, and the resulting stresses and error are compared in Table (2) and Table (3). It should be noted that (A) corresponds to stresses at a node along the same cross section as the load and (B) corresponds to a stress that is located on a node in half-way between point loads. The magnitude of each point load remains the same 300 pN, and the error is calculated by comparing stress values at nodes located midway (90°) and one quarter the way (45°) down the side of the microtubule under the point loads to that of nodes that are centrally located in-between point loads, as illustrated in

Figure (18). In this scenario, it can be seen as the spacing between loads increases by a factor of

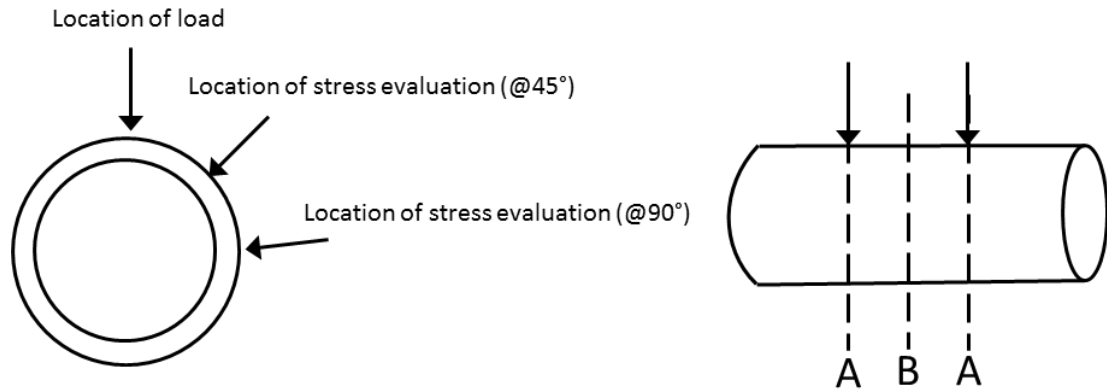


Figure 18. Illustration of locations of stress evaluation.

2, that the stresses roughly decrease by 2. Also, the error in stress difference along the midway section is much less dependent on spacing as the quarter way stresses, which start to become significant at a load spacing of 16.7 nm or approximately the diameter of the MT.

Table 2. Von Mises stress as point load spacing varies at 90°

Load Spacing (nm)	(A) $\sigma_{\text{von}} @ 90^\circ$ (MPa)	(B) $\sigma_{\text{von}} @ 90^\circ$ (MPa)	Error @ 90° (%)
2.08	249.9	249.9	0.0
8.33	123.1	123.0	0.0
16.67	52.3	59.5	0.2
25	32.4	32.6	0.7

Table 3. Von Mises stress as point load spacing varies at 45°

Load Spacing (nm)	(A) $\sigma_{\text{von}} @ 45^\circ$ (MPa)	(B) $\sigma_{\text{von}} @ 45^\circ$ (MPa)	Error @ 45° (%)
2.08	49.7	49.7	0.0
8.33	25.7	26.1	1.6
16.67	14.6	15.3	5.2
25	14.2	16.4	15.1

Next, the magnitude of the force is scaled accordingly in each spacing scenario to match the same 250 MPa Von Mises stress that was found on the outer side of the MT. In this simulation, only the stresses located midway down the side of the MT were considered. From those simulations the magnitudes, spacing, and error can be found in Table (4). Here the stresses at the 45 degree location are not included. It can be seen that as the spacing between loads is doubled, that the force needed to maintain the same stresses approximately doubles as well, as expected. From these results, it can be seen that a load spacing equivalent to the diameter of the MT is adequate in representing distributed loading. Such information would be useful in future experimental efforts where a simulated distributed loading is to be mimicked through the application of multiple point loads.

Table 4. Loads needed to maintain a constant Von Mises stress

Force (pN)	Load Spacing (nm)	(A) $\sigma_{\text{von}} @ 90^\circ$ (MPa)	(B) $\sigma_{\text{von}} @ 90^\circ$ (MPa)	Error @ 90° (%)
300	2.08	249.9	249.9	0.00
609	8.33	249.9	249.9	0.00
1265	16.67	249.9	249.9	0.18
2315	25.00	249.9	248.2	0.69

Observing that the PL model has large stresses around the location of the load, the Rigid Plate (RP, Figure 7) model with loading that creates the same y-direction stresses along the outer side of the MT as determined in the PL model was examined. The RP serves as an aide in beginning to better understand the loading mechanics that were present in the AFM experiments. Initially a 6 MPa pressure load is applied, which has resulting extreme y-stresses of -716 MPa and 561 Mpa. To generate the same y-direction stresses as the PL model, the pressure is adjusted until the RP model gives similar stress results. It can be seen that the extreme y-direction stresses occur at the same location of the MT as in the PL model as seen in Figure (19) and result from a 0.238 MPa applied pressure. The values in the y-direction stresses that occur in the same location evaluated in the PL model are 22.26 MPa and -28.40 MPa respectively. Comparing the

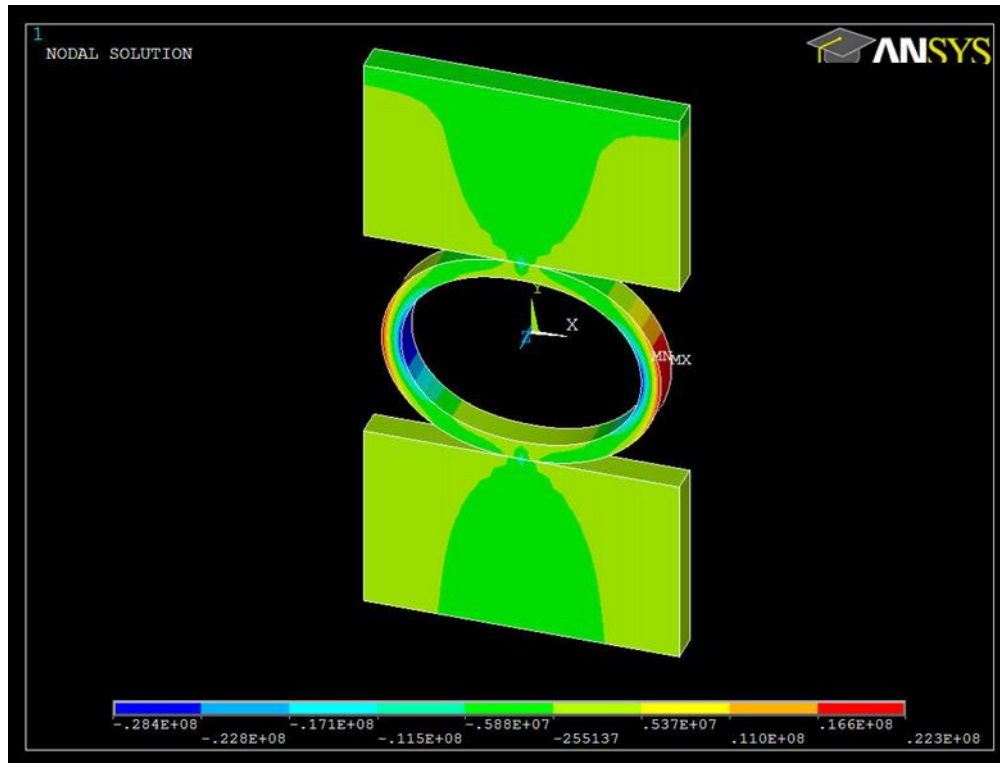


Figure 19. Y-direction stress distribution of RP model.

average between the maximum and minimum PL y-stresses to those of the RP model, it can be seen that they both share an average of 25.3 MPa. Of course, this result is as expected. Also, in comparing the z-direction stresses (not shown) located at the same nodes as the extreme y-direction stress, there is an approximately 400 percent increase from the PL model to the RP model. However these z-direction stresses that are being compared are only 6 to 30 percent of the y-direction stresses. From the RP model, it can be seen that the extreme y-direction stresses are important characteristics in determining failure criterion for microtubules due to their comparably higher magnitudes. This observation gives a starting point for determining a sufficient applied load for the models that require a pressure instead of a force.

When considering in cylindrical coordinates, the RP model produces a maximum tangential stress of 44.1 MPa, which occurs on the inner top surface of the microtubule. A minimum tangential stress of -45.6 MPa occurs on the outer bottom of the MT. The associated stresses distribution of the RP model can be seen in Figure (20). The tangential stresses in the RP model result in a symmetric stress distribution along the wall of the tube section. Although not shown, the maximum and minimum radial stresses occur at these same locations and their values are 2.2 MPa and -14.2 MPa, respectively.

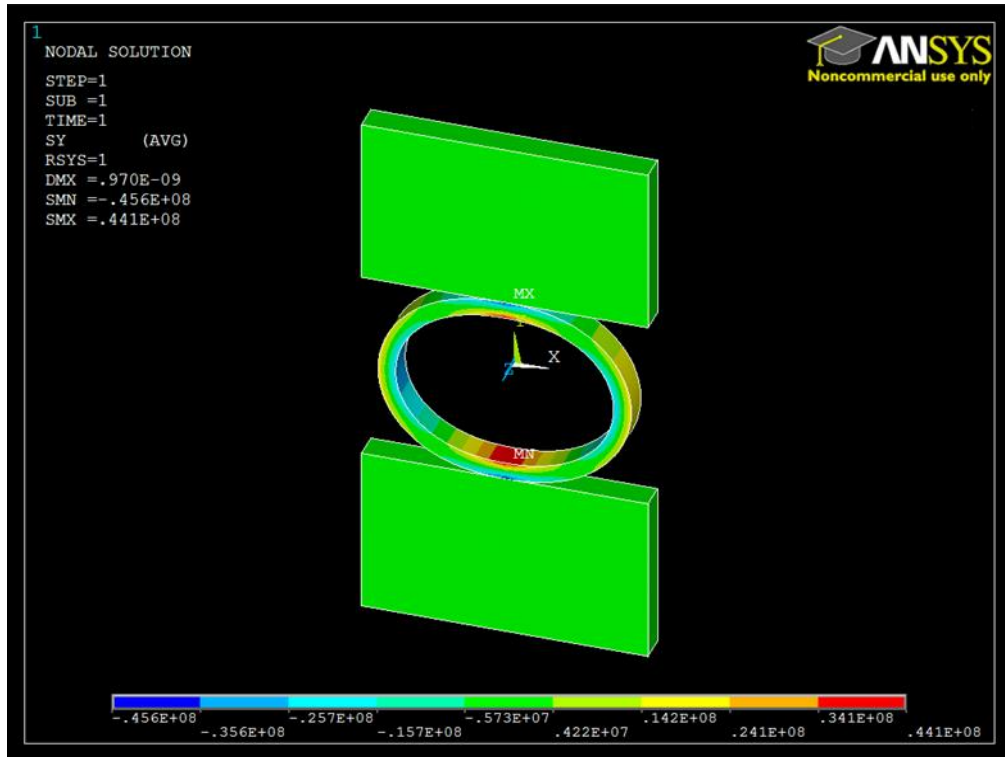


Figure 20. Tangential stress distribution of RP model.

The AFMSE model, Figure (8), is originally analyzed with a load of 3.75 MPa, which produces a load of 300 pN on the upper surface of the AFM tip. This load produces extreme y-direction stresses that occur at the same location of the previous models as illustrated in Figure (21). The values of the maximum and minimum stresses are very large when compared to those of the PL and RP models. This is, however, expected due to the fact that symmetry is being imposed and the total load on the MT will be significantly larger than a real MT would experience from an AFM tip. The point of this model, though, is to move towards determining what distributed loads impact the MT in the same manner as an AFM load.

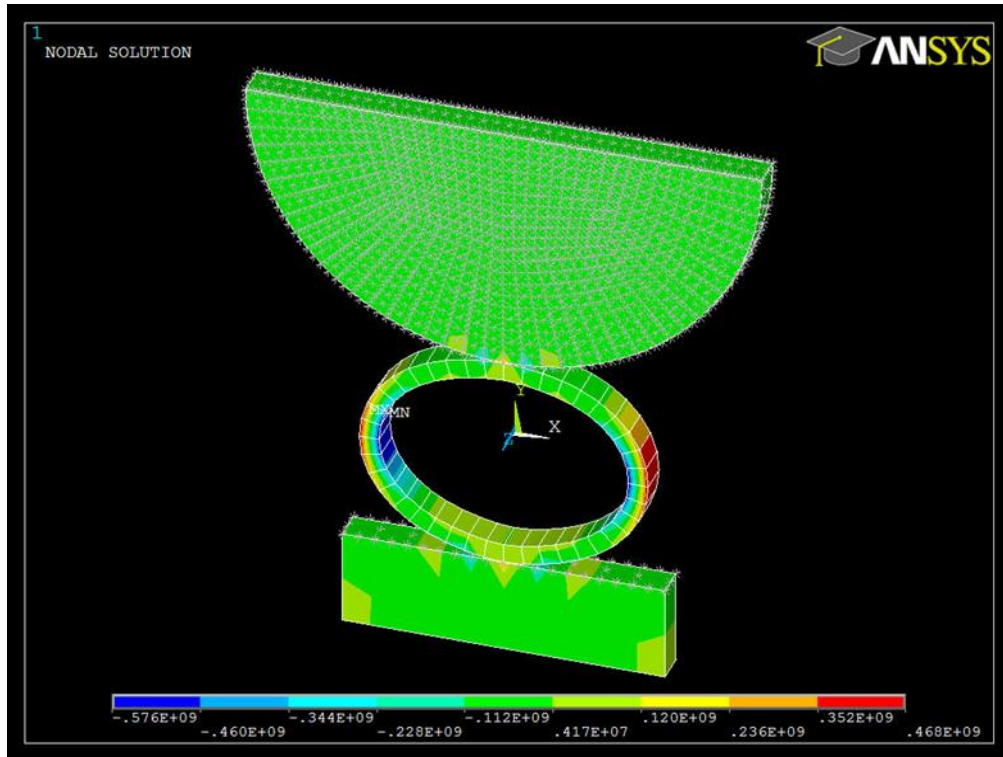


Figure 21. Y-direction stress distribution of the AFMSE model with 3.75 MPa load.

Since this model was created to determine what loads impact in the same manner as the previous models, the 0.238 MPa pressure is scaled based on the relative width of the AFM tip in comparison to the plate in the RP model. This scaled pressure, 0.148 MPa, produces extreme stresses of -22.8 MPa and 18.6 MPa. The stresses associated with this new pressure loading can be seen in Figure (22). When compared to the results of the PL and RP models, the y-stresses found in the AFMSE model are approximately 18 percent smaller. Also, the z-direction stressed at the same nodes show a similar 18 percent decrease while the x-direction stresses differ by 200 percent.

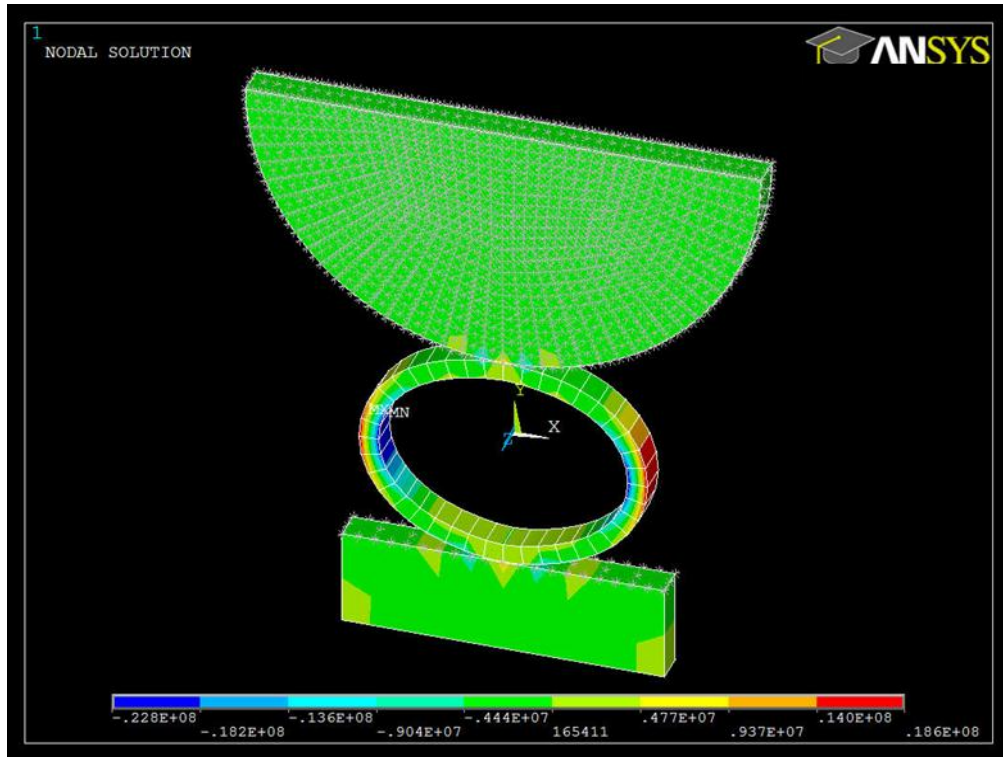


Figure 22. Y-direction stress distribution of the AFMSE model with 0.148 MPa load.

For the AFMSE model, these correspond to maximum and minimum tangential stresses of 43.4 MPa and -43.2 MPa, respectively. These stresses can be seen in Figure (23). Also the maximum and minimum radial stresses are 2.1 MPa and -5.9 MPa, respectively. These tangential and radial stress maximums occur at the same locations as seen in the RP model, the inner top surface and outer bottom surface of the MT. It can be noted that the average tangential stress in the AFMSE model is approximately 3.5 percent smaller than that of the RP model.

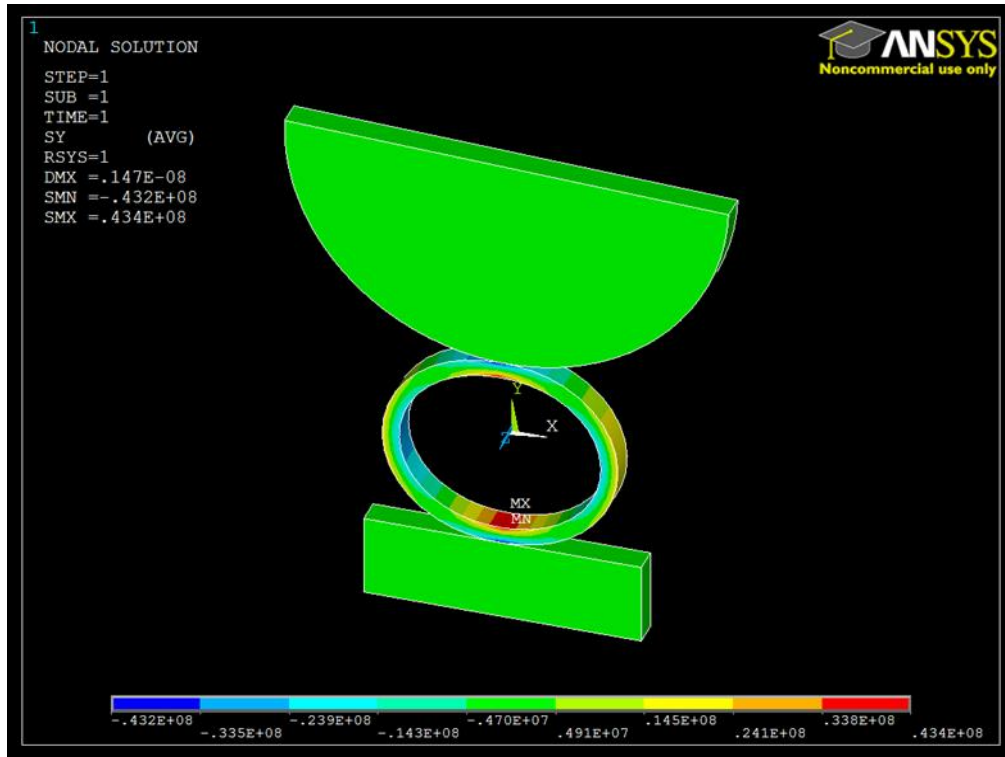


Figure 23. Tangential stress distribution of the AFMSE model.

To further examine the effect of the tip radius on the microtubule response, the AFMF model enables study of a finite length tube in contact with a more true depiction of the AFM tip. With an area based load of 0.238 MPa applied to the top surface of the tip, the maximum y-direction stress occurs at the point where the AFM tip contacts the MT. That stress is 20.9 MPa as seen in Figure (24).

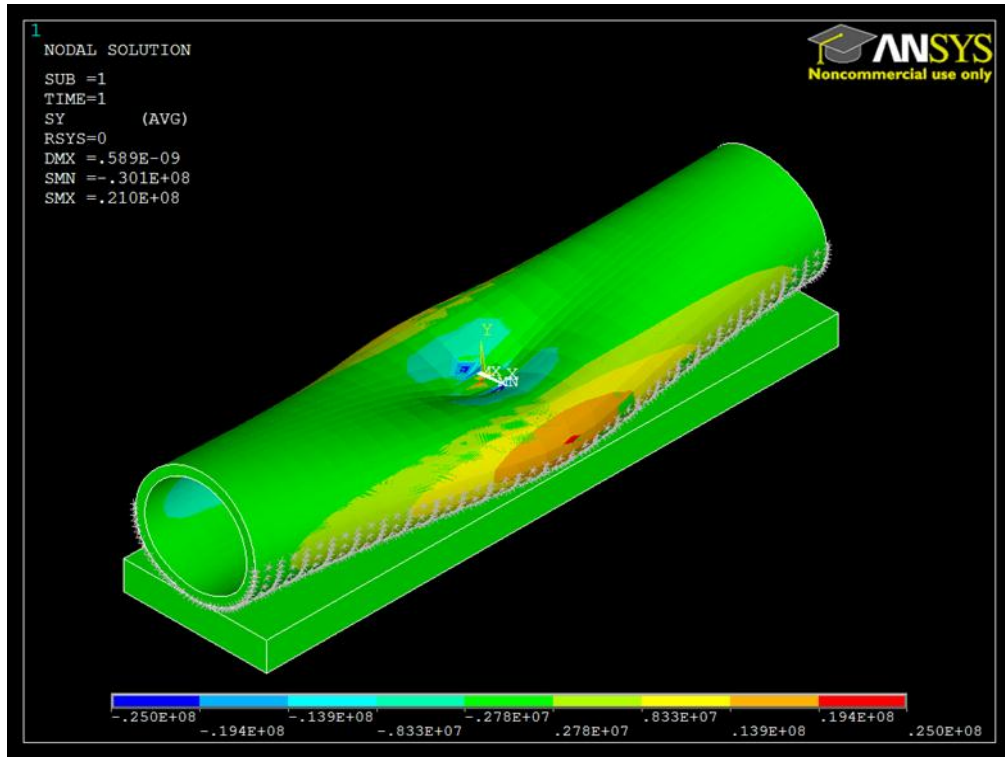


Figure 24. Y-direction stress distribution of the AFMF model.

When compared to other models, the y-direction stress on the side of the MT is 17.8 MPa for this model. The minimum y-direction stress occurs inside the tube directly below the maximum stress, and has a corresponding value of -30.1 MPa. Taking the average of the extreme values of the AFMF model and comparing it to the average values found in the PL, RP, and AFMSE models, the AFMF model's average is approximately within 1 percent of these model's averages. The AFMF model gives extreme tangential stresses of 54.3 MPa and -84.1 MPa on the area where the AFM tip contacts the upper surface of the MT. The resulting tangential stresses can be seen in Figure (25). When compared to the average extreme y-direction stress magnitudes, the tangential stresses that arise in the AFMF model are approximately 170 percent higher. The extreme radial stresses, which are not displayed, have a

corresponding maximum and minimum of 21 MPa and -10.2 MPa, respectively and are located at the location where the tip contacts the tube.

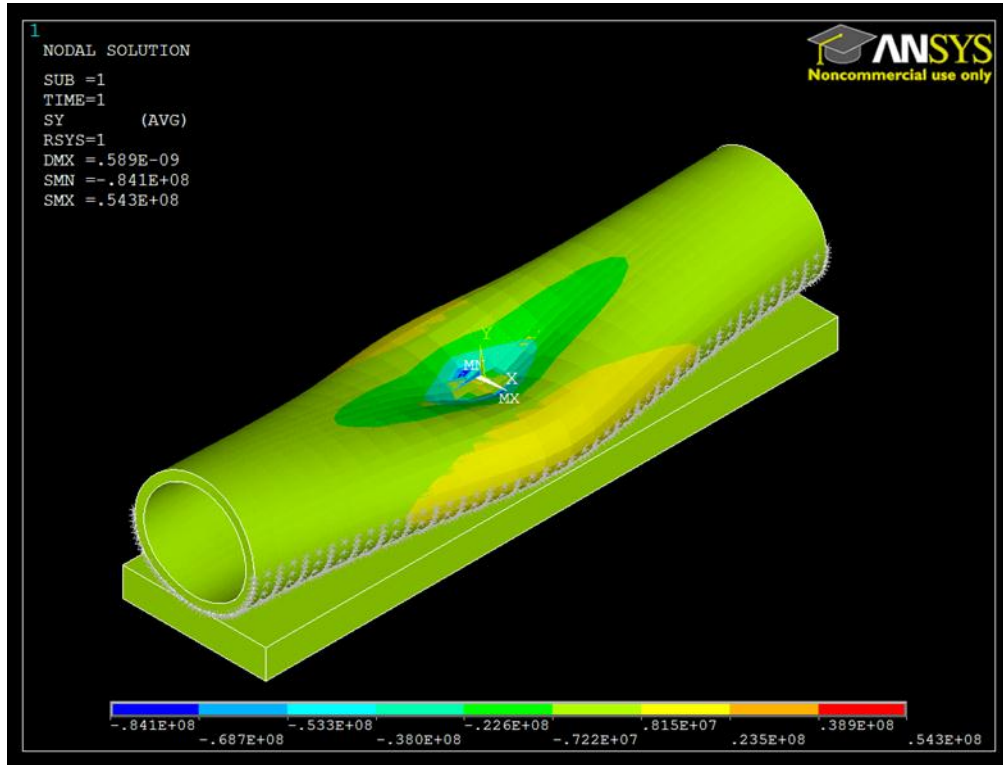


Figure 25. Tangential stress distribution of the AFMF model.

The above models show that the resulting stresses in the y-direction and stresses in the tangential direction are likely candidates for a structural failure criterion. These stresses are due to combined bending stresses and axial loading stresses in the vertical direction that occur on the sides of the MT. Furthermore, with equivalent loading these models all share approximately the same y-direction stresses at the same locations.

IN VIVO STATIC STUDIES

The previous models represent the loading mechanics of microtubules when the configuration is representative of *in vitro* conditions. In order to extend the insight gained above

and to account for an *in vivo* scenario, the Composite Single Element (CSE, Figure 10) model is used. A 0.12 MPa load, an arbitrary value, is initially applied to the top surface of the cytoplasm.

As noted in a previous chapter, it is first important to determine what spacing dimensions to the boundaries should be used for the desired type of loading. In order to quantify the impact that neighboring MTs have on the resulting MT stress distribution, the distance between the boundary and the MT structure is adjusted. Figure (26) shows the impact of the horizontal spacing between microtubules on the maximum von Mises stress at the same locations in the microtubule. Note that in this simulation, the lower boundary is sufficiently far away to eliminate its impact on the MT stress (see discussion below). As can be seen in the figure, a nearby MT does not begin to impact the stresses until the MTs are closer than about 80 nanometers. As the distance between MTs decreases, the maximum von Mises stress in the MT increases. This increase in the stress is due to the fact that more of the loading is carried by the microtubules due to the increase in overall structure stiffness. This stiffness increase is due to the increased density of MTs within the relatively soft cytoplasm. When the spacing is greater than the 80 nm, the cytoplasm is bearing most of the load.

It has been found in other research that motor proteins that interconnect microtubules provide a range in spacing of approximately 10 nm to 20 nm between connected MTs (13 ,14). As a result, this simulation shows that stresses seen in MTs within the axon may be slightly higher when motor proteins connect those MTs. Therefore, distributed loading within the brain might produce a separation of motor proteins from the connected MTs. More importantly, those MTs connected by motor proteins might be more likely to experience structural failure. The

associated increase in stress within MTs that are connected by motor proteins ranges from approximately 2 to 4 percent, depending on the size of the motor protein.

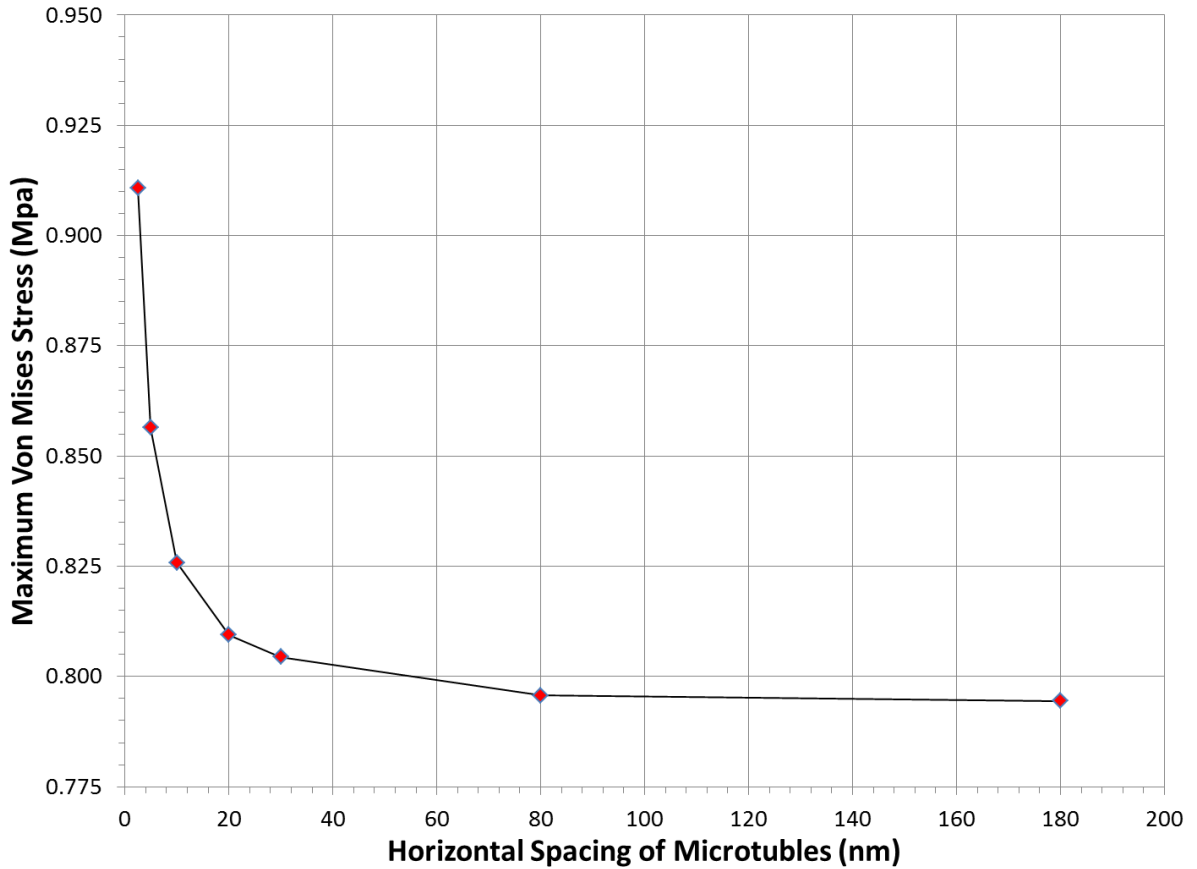


Figure 26. Impact of horizontal spacing on maximum von Mises stresses in adjacent MTs.

To examine the impact of a nearby rigid boundary, Figure (27) shows the influence of the vertical spacing of MTs relative to the lower rigid boundary condition on the maximum von Mises stress at the same locations on the tube. It can be seen in the figure that the rigid boundary's location in relation to the microtubule has a small impact on the stress with the MT. The associated increase in the overall von Mises stress that occurs as the rigid boundary distance decreases from 60 nm to 2.5 nm is only about 6 percent. From this, it can be seen that the rigid

boundary location in relation to the MT has little effect on the Von Mises stresses of the MT. By understanding the impact that a rigid surface could have, it may be possible to better understand how the presence of nearby structures, like bone, for example, could affect stresses within the MT.

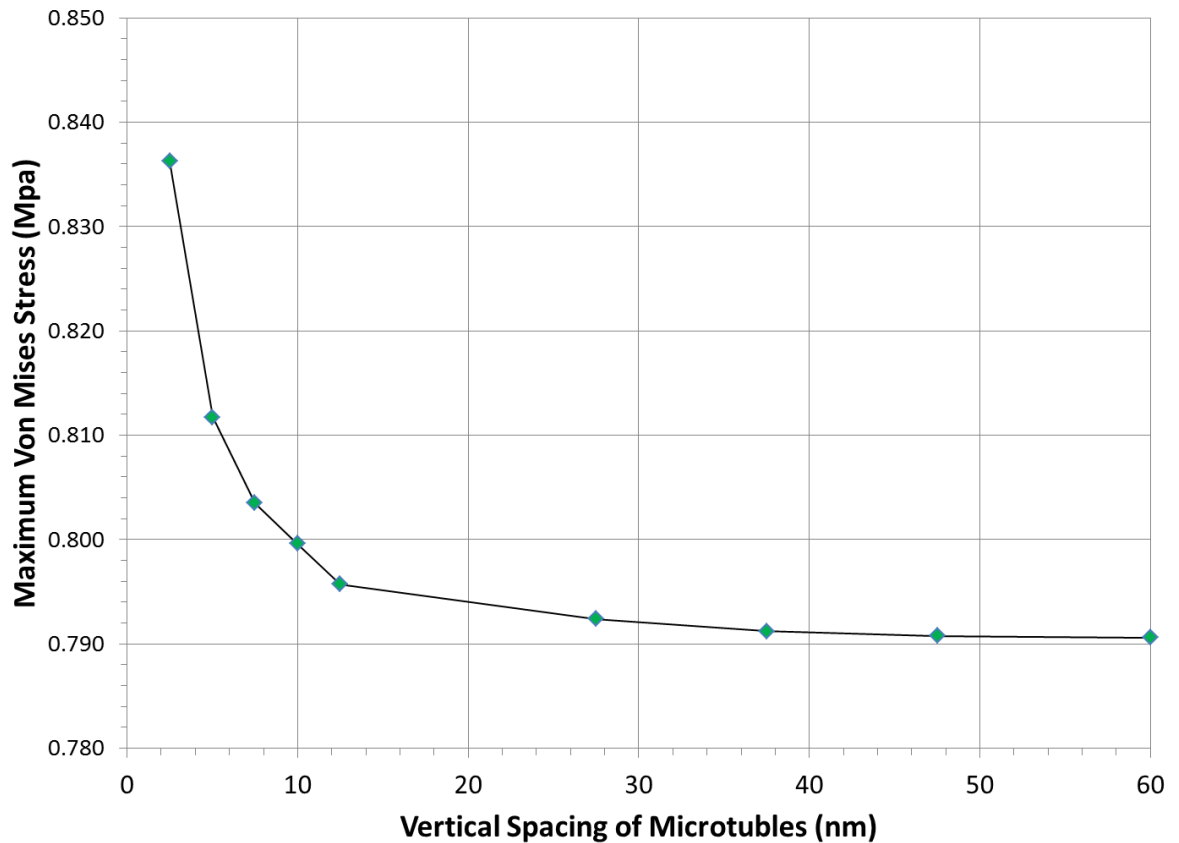


Figure 27. Impact of vertical spacing on maximum von Mises stresses in MTs near a rigid surface.

In addition to evaluating the impact of nearby microtubules and rigid boundaries, the CSE is also used to gauge the y-direction stresses that arise as a result of pressure loading. By using the results of the spacing analysis, a model utilizing boundary distances found above that do not affect the stresses was generated. This model has a horizontal boundary set at 80 nm and

a bottom rigid boundary at 50 nm. In this model, seen in Figure (28), a load is applied until the y-direction stresses match those of the PL, RP, AFMSE, and AFMF models. In this case, a static pressure of 3.75 MPa is needed, which results in a minimum y-stress of -28.1 MPa at the interior of the side of the MT. However, in the same model (CSE) the maximum y-stress is 0.01 MPa, which in comparison is much smaller than the resulting maximums that occurred in all previous models. This decrease in the maximum y-stress results from the cytoplasm sharing the applied load and changing the stress characteristics in the MT. In addition, the load was scaled to 11.4 MPa to match the minimum tangential stress of -84.1 MPa seen in the AFMF model. This

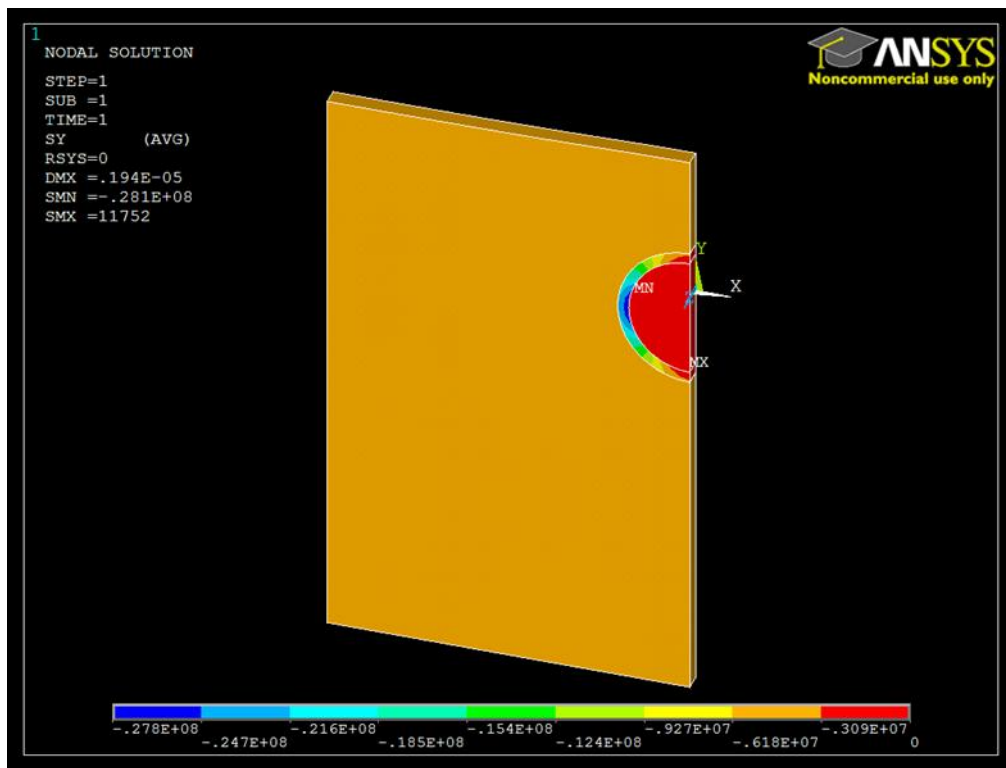


Figure 28. Y-directions stress distribution of the CSE model.

loading produces maximum tangential and radial stresses of approximately zero. The corresponding minimum tangential stress is -84.1 MPa while the minimum radial stress is -11.3

MPa. The tangential stress distribution of the CSE model can be seen in Figure (29). When the minimum radial stress is compared to the minimum seen in the AFMF model, the CSE model's minimum is approximately 10 percent higher.

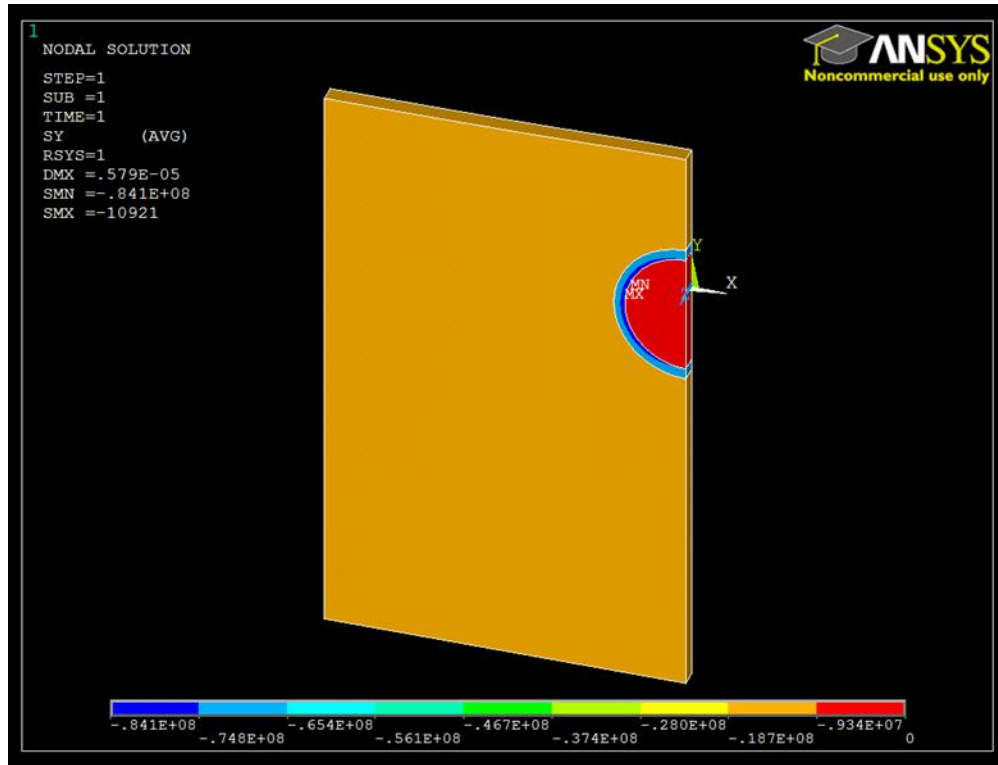


Figure 29. Tangential stress distribution of the CSE model.

It can be seen that the cytoplasm plays an important role in the mechanical loading characteristics of microtubules. On the other hand, the resulting negative y-direction bending stress, the minimum tangential stress, and the minimum radial stress present in the interior of the MT could play a significant role in the determination of failure criterion of MTs. In the CSE model, though the axial loading components in the vertical direction outweigh the bending components.

IN VIVO TRANSIENT STUDIES

The next step was to take the CSE model and view the effects of transient pressure loading. To start with, the natural frequencies, f_n , of a plain *in vitro* tube were calculated as well as the natural frequencies of the *in vivo* CSE model. These frequencies were used to set the foundation for the transient pressure wave simulation as well as understand the mode shapes that were present in both cases. The first 10 cross-sectional natural frequencies, f_n , of each case can be seen in Table (5), where the *in vitro* is the natural frequencies of a free microtubule and the *in vivo* is the combined natural frequencies of a microtubule and cytoplasm. Here the f_n 's of the *in vivo* listed correspond to mode shapes of the cytoplasm, and to attain the f_n 's of the MT would require consideration of many more modes due to the high value of the *in vitro* MT modes relative to those in the cytoplasm modes where the MT behaves rigidly. Also, note that the free (*in vitro*) MT has rigid body modes with zero frequency.

Table 5. Natural frequencies of in vitro and in vivo MT cross section.

Number of w_n -	f_n of in vitro (Hz)	f_n of in vivo (MHz)
1	0	5.7
2	0	9.1
3	0	10.8
4	5440.4	11.4
5	8465.3	12.9
6	12358	13.8
7	2.38E+09	15.2
8	2.38E+09	16.3
9	2.86E+09	17.3
10	2.86E+09	17.4

To begin the transient pressure analysis, time range of 2 milliseconds with a time step of 20 microseconds was initially used, which was based off shock tube experiments where the blast duration is on the order of 2 milliseconds (25). From (25), the excitation frequency, f , in a blast event is therefore on the order of 500 Hz. When compared to the natural frequency, f_n , of the *in vivo* study, $f \ll f_n$. The relationship between the two frequencies compared to the overall magnitude of the response is given by Equation 1:

$$\left| \frac{x}{F/s} \right| = \frac{1}{1 - \left(\frac{f}{f_n} \right)^2} \quad (1)$$

This correlation between the excitation frequency and natural frequencies results in a response

similar to static loading, i.e. $\frac{1}{1 - \left(\frac{f}{f_n} \right)^2} \sim 1$. This information is useful in correlating a static to transient loading. From this, one can assume the use of static loading to experimentally evaluate the response of microtubules given their very high cross-sectional natural frequencies. Furthermore from this simulation, the results of this time scale resembled the static loading case identically and the pressure wave was passing through the model so quickly that wave propagation within the MT was difficult to visualize. To further understand what loading is taking place, a new time scale is needed to capture the pressure wave as it passes through the MT. For a starting point, the calculated speed of sound for the cytoplasm (12.7 m/s) is used to establish a time scale for the transient modeling. Since the CSE model has a total length of 85 nm, a time scale of 6.08×10^{-9} sec is subsequently used, which is approximately the time needed for the wave to cross the dimension of the model one time. At this time scale, the step input wave has a fundamental frequency of roughly 150 MHz, which is well above the natural frequencies listed in Table (5) for the cytoplasm but well below the vibratory modes for the *in*

vitro MT (mode 7 and higher). Initially an arbitrary step input pressure is used to find which instant in time the minimum tangential stress occurs in the MT, which is at 1.41×10^{-9} sec. This is done such that the minimum tangential stress, -84.1 MPa, seen in the AFMF model can be matched. The pressure is scaled to a magnitude of 1.25 MPa, which results in a maximum tangential stress of 84.6 MPa and minimum of -84 MPa. This type of stress distribution is like that of the static AFMF model and can be seen in Figure (30). In comparing the transient results to the static results, it can be seen that the pressure needed in the transient loading was approximately 800 percent lower to that of the static pressure.

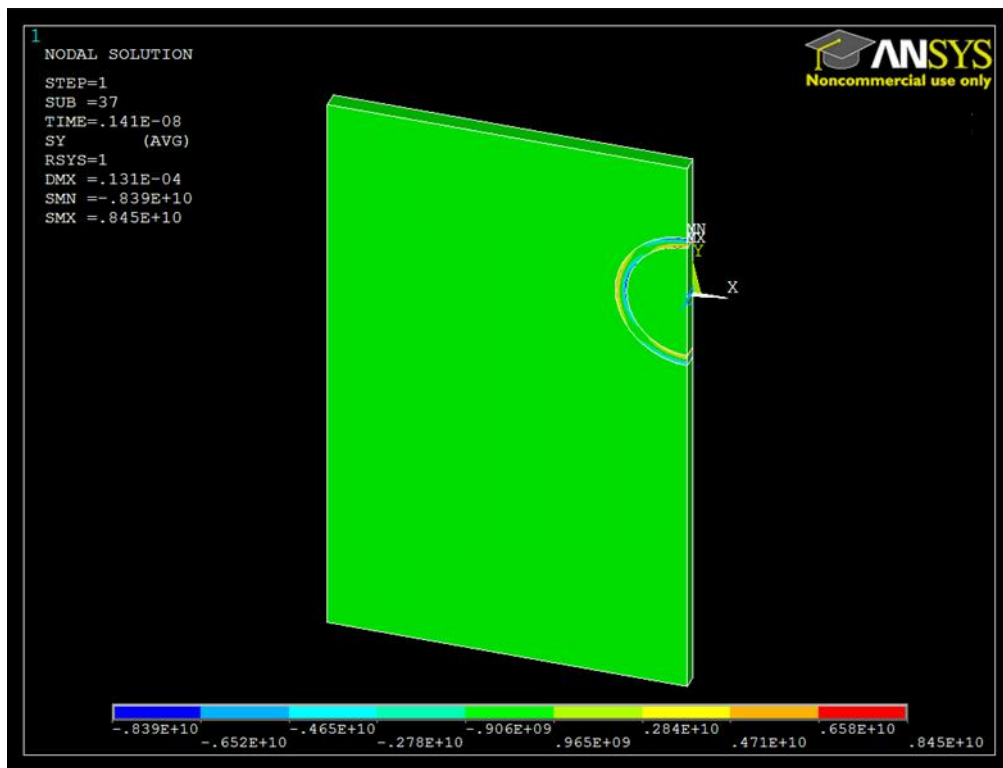


Figure 30. Tangential stress distribution of the transient CSE model.

Next, to model a more realistic blast event, another transient simulation was created. With the goal of matching the same minimum tangential stress, an impulse wave with a 6.9 MPa

positive front and a 3.45 MPa negative was used. Both magnitudes were applied over a time step of 3.8×10^{-11} sec and the pressure wave was evaluated over a total time range 6.08×10^{-9} sec. As noted earlier, the resulting frequencies associated with this excitation are quite high, on the order of 10 GHz. While such a wave does not have a physical counterpart, it does allow us to investigate wave propagation through the MT cross-section. This shock wave scenario resulted in a maximum tangential stress of 74.6 MPa and a minimum tangential stress of -84.1 MPa at a time of 1.44×10^{-9} sec.

To further examine the *in vivo* conditions, a transient case consisting of vertical point loads (Figure 12) along the top most nodes of the microtubule in the CSE model was created. The time scale was the same as used in the transient pressure version, which is a total time of 6.08×10^{-9} sec. Initially these loads had a magnitude of 300 pN, which caused the minimum tangential stress to exceed the -84.1 MPa seen in the AFMF simulation. Thusly, the magnitude of the point loads was scaled until these stresses matched. In addition to loading the MT at the top (case 1), it was also loaded at the top and at 90 degrees down the side simultaneously (case 2), and finally with 3 point loads simultaneously, one at top, 45 degrees and 90 degrees (case 3). The results of these loading scenarios are summarized in Table (5).

Table 5. Transient point loads.

Case	Time (sec)	Load (N)	Max σ_T (MPa)	Min σ_T (Mpa)
-	2.66E-	7.29E-		
1	10	12	78.0	-84.1
2	2.28E-	1.10E-	69.5	-84.1
	10	11		
3	2.28E-	1.13E-	71.4	-84.1
	10	11		

SUMMARY

In this chapter the results of the all of the simulations were presented. The three different studies, *in vitro* static, *in vivo* static, and *in vivo* transient were discussed. The *in vitro* static study consisted of the PL, PLP, RP, AFMSE, AFMF models. These *in vitro* models paved the way to understand further the loading mechanics of the AFM experiments and to correlate them to a more realistic transient blast event. It was shown that that with a point load spacing that is less than the diameter of the MT, the resulting stresses along the MT resemble that of distributed loading. From the results of these models, a comparison was made to the *in vivo* static model, which was the CSE model. Here boundary effects as well a loading stress comparison was made to the aforementioned *in vitro* models. It was shown that a MT spacing of a distance greater than 80 nm and a rigid boundary spacing of 50 nm did not impact the resulting maximum Von Mises stresses. Once an understanding was gained, a transition from *in vivo* static to *in vivo* transient was made. This study allowed for an examination of transient wave propagation and also, what natural frequencies are present in the microtubule cross-section.

CHAPTER 4

CONCLUSION

In previous modeling studies, traumatic brain injury has been evaluated from a macroscopic point of view and axonal injuries have been examined only through the computation of stresses, strains, and strain rates. The approach taken in those studies has been with assumed homogeneous material properties for the white and gray matter. The research presented here numerically studies brain injury from a microscopic perspective, focusing on the mechanical response characteristics of microtubules. The ultimate goal of the research is to determine a loading threshold for mild traumatic brain injury. Using loads found by other researchers that result in permanent microtubule damage during atomic force microscopy experiments, an analysis using finite element models is conducted in this research. These models include the Point Load (PL), Rigid Press (RP), Atomic Force Microscopy Single Element (AFMSE), Atomic Force Microscopy Full (AFMF), and the Composite Single Element (CSE). The PL model examines the assumption of a point load and provided y-direction stresses to be used for comparison purposes. The RP model is used to match the results of the PL model and required a distributed load of 0.238 MPa to accomplish that matching. In the AFMSE model, this 0.238 MPa load was scaled based on the relative width, which gave y-direction normal stresses that were 18 percent lower than the RP model. The AFMF model captures a more accurate depiction of the AFM experiments and gives insight to the relation of the AFM tip and the extreme stress magnitudes. The CSE model was initially used to shed insight on the impact

of nearby microtubules. That study showed that stresses begin to increase as the distance between MTs decreases below 80 nm, although the increase is not necessarily significant. Furthermore, since it is known that the relative MT spacing provided by the motor proteins is approximately 10 to 20 nm, the expected stresses within the MT will be higher when a motor protein has joined two MTs. It was also shown that when point loads are imposed on the top surface of the MT are spaced less than the MT diameter, the loading mimics that produced by a distributed load. Also, with the transient pressure loading, the microtubule stress distributions behave more like that of the AFMF static model. This relationship can allow one to use static loading to correlate structural response of MTs.

FUTURE RESEARCH

For the models and simulations examined in this work, only the cross sectional loading of microtubules was considered. In future work, longitudinal wave propagation within microtubules would be a point of interest. A comparison then could be made from cross sectional to longitudinal transient behavior. Another topic of interest from an experimental perspective would be to develop loading methods in the lab that well simulated the distributed loading associated with a blast pressure wave.

REFERENCES

1. *Traumatic Brain Injury in the United States: Emergency Department Visits, Hospitalizations, and Deaths* (2007), Retrieved March 12, 2011, from http://www.cdc.gov/ncipc/pub-res/TBI_in_US_04/TBI_ED.htm
2. <http://www.passenlaw.com>
3. P. A. Taylor, C. C. Ford, "Simulation of early-time head impact leading to traumatic brain injury," *International Neurotrauma Letter.*, 1, (2007).
4. http://emergency.cdc.gov/coca/ppt/09_21_10_DeploymentHealth_INT4.pdf
5. Y. Bhattacharjee, "Shell shock revisited: Solving the puzzle of blast trauma," *Science*, 319, pp. 406-408 (2008).
6. S. Kleiven, "Evaluation of head injury criteria using a finite element model validated against experiments on localized brain motion, intracerebral acceleration, and intracranial pressure," *I. J. Crash.*, 11(1), pp. 65-79 (2006).
7. S. G. Waxman, J. D. Kocsis and P. K. Stys, *The Axon: Structure, Function, and Pathophysiology*, p. 692 (1995).
8. A. Brown, "Slow axonal transport: stop and go traffic in the axon," *Nat. Rev. Mol. Cell Biol.*, 1(2), pp. 153-156 (2000).
9. F. Gittes, B. Mickey, J. Nettleton and J. Howard, "Flexural rigidity of microtubules and actin filaments measured from thermal fluctuations in shape," *J. Cell. Bio.*, 120(4), pp. 923-934 (1993).
10. D. Sept and F. C. MacKintosh, "Microtubule elasticity: Connecting all-atom simulations with continuum mechanics," *Physical Rev. Letters*, 104(1), pp. 018101-1-4 (2010).
11. I. A. T. Schaap, C. Carrasco, P. J. de Pablo and F. C. MacKintosh, "Elastic response, buckling, and instability of microtubules under radial indentation," *Biophysical J.*, 91(4), pp. 1521-1531 (2006).
12. P. J. de Pablo, I. A. T. Schaap, F. C. MacKintosh and C. F. Schmidt, "Deformation and collapse of microtubules on the nanometer scale," *Physical Rev. Letters*, 91(9), pp. 098101-1-4 (2003).

13. Hunt, A. J.; Howard, J. Proc. Natl. Acad. Sci. U.S.A. 1993, 90, 11653-11657
14. Miller, R.; Lasek, R. J. Cell Biol. 1985, 101, 2181-2193.
15. Zhang, B., Shepard, W. S., “Investigation of stress wave propagation in brain tissues through the use of finite element method,” IMECE2010-39994 (2010).
16. Buki, A., and Povlishock, J. T., 2006, “All Roads Lead to Disconnection? – Traumatic Axonal Injury Revisited,” *Acta Neurochir. Suppl. (Wein)*, 148(2), pp. 181-193.
17. P. A. Taylor, C. C. Ford, “Simulation of Blast-Induced Early-Time head impact leading to traumatic brain injury,” *Journal of Biomechanical Engineering*, Vol 131. (2009).
18. Harrigan, T.P., Roberts, J.C., Ward, E.E., & Merkle, A.C. (2010). Correlating Tissue Response with Anatomical Location of mTBI Using a Human Head Finite Element Model under Simulated Blast Conditions, *International Federation for Medical and Biological Engineering Precedings*, 32, 18-21.
19. Howard, J., (2001). *Mechanics of Motor Proteins and the Cytoskeleton*. Sunderland, MA: Sinauer Associates, Inc.
20. Brown, A., (2000). *Slow axonal transport: stop and go traffic in the axon*. Retrieved March 12, 2011, from <http://www.neurobiotech.ohio-state.edu/brownlab/docs/Brown2000.pdf>
21. Kamal, A., Goldstein, L. S. B. (2002). Principles of cargo attachment to cytoplasmic motor proteins. *Current Opinion in Cell Biology*, 1. 63-68.
22. P. J. de Pablo, I. A. T. Schaap, F. C. MacKintosh and C. F. Schmidt, “Resolving the Molecular structure of microtubules under physiological conditions with scanning force microscopy,” *Biophysics Letters*, 33, pp. 462-467 (2004).
23. Conde, C., Caceres, A. (2009). Microtubule assembly, organization and dynamics in axons and dendrites. *Nature Reviews Neuroscience*, 10. 319-332.
24. Baal, P. W., Black, M. M. (1990). Individual microtubules in the axon consist of domains that differ in both composition and stability. *The Journal of Cell Biology*, 111, 395-509.
25. Courtney, M. W., Courtney, C. C. (2010). A table-top blast driven shock tube. *Review of Scientific Instruments*. 80.
26. Jiang, H., Zhang, J. (2008). Mechanics of Microtubule Buckling Supported by Cytoplasm. *Journal of Applied Mechanics*, 75, (061019-3).
27. Young, W. C. (1989). *Roark's Formulas for Stress & Strain* (6th Ed.), NY: McGraw-Hill

APPENDIX

ANALYTICAL SOLUTION

Most of the models used in this research do not fit the conditions used to generate analytical models found in the literature. Nevertheless, there are some conditions which can be compared with analytical results to ensure that the boundary conditions and loads are correctly implemented within the finite element model. The PLP model is one such case that will be described here.

From the numerical analysis of the PLP Model conducted in Ansys, the maximum bending stress that occurs at the 90° location on the microtubule (at the neutral axis) was found to be 147.9 MPa. This number was determined by adding the magnitude of the stress value at the outer node to the magnitude of the stress value at the inner node and then dividing the sum by two. By doing this, the axial stress component is removed from the total stress, leaving just the bending stress component.

Since the distributed point loads along the top essentially generate a uniform model, the bending stress can also be computed analytically using the equations give in Roark (27). The finite element model geometry and the Roark simplification are illustrated below in Figure (31)

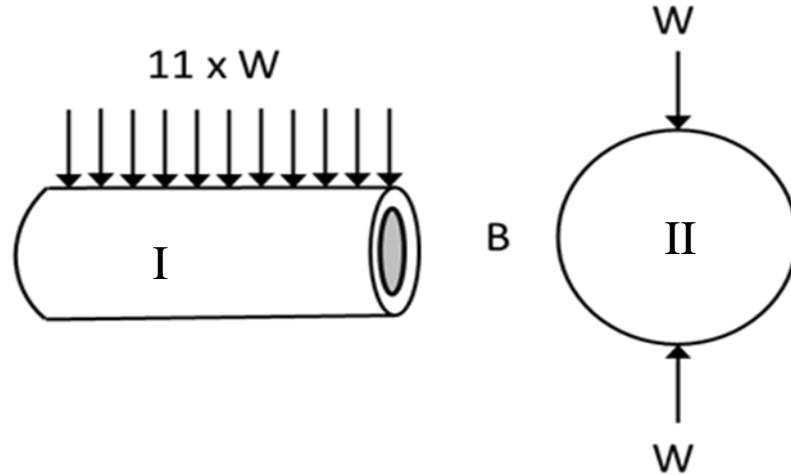


Figure 31. (I) PLP model. (II) Roark ring under concentrated point load

To that end, a microtubule which has a length (b) of 100 nm, outer radius (R) of 19.88 nm, and a wall thickness (t) of 1.54 nm is examined. Using the moment equation found in Table 17 of (27)

$$M_B = -(0.5 - 0.3183k_2)WR$$

where W (3.3 μN) is the total load, R (19.88 nm) is the radius of the cylinder and k_2 is defined as

$$k_2 = 1 - \frac{I}{AR^2} .$$

In the above equations, $A=(b*t)$ is the area, R is the radius of the cylinder, and I is defined as

$$I = \frac{bt^3}{12}$$

The bending stress at this location can then be found using the standard equation for bending stress

$$\sigma_B = \frac{M_B t/2}{I}$$

The resulting bending stress was computed to be 151.3 MPa and when compared to the numerical version of the solution, the difference in the stresses is approximately 2.2%. It should be noted that the total load of 3.3 μN is representative of 11 equally spaced point loads over the 100 nm length of the tube. The distributed point loads in the finite element model do not exactly represent a true distributed load. As a result, it is not surprising that there is some small difference between the finite element result and the analytical solution. If the spacing of the point loads were subsequently reduced and the magnitudes adjusted accordingly, it is expected that the overall numerical stresses will converge closer to the analytical value computed above. However, the results under the current configuration are quite close.

NUMERICAL SOLUTION CONVERGENCE STUDY

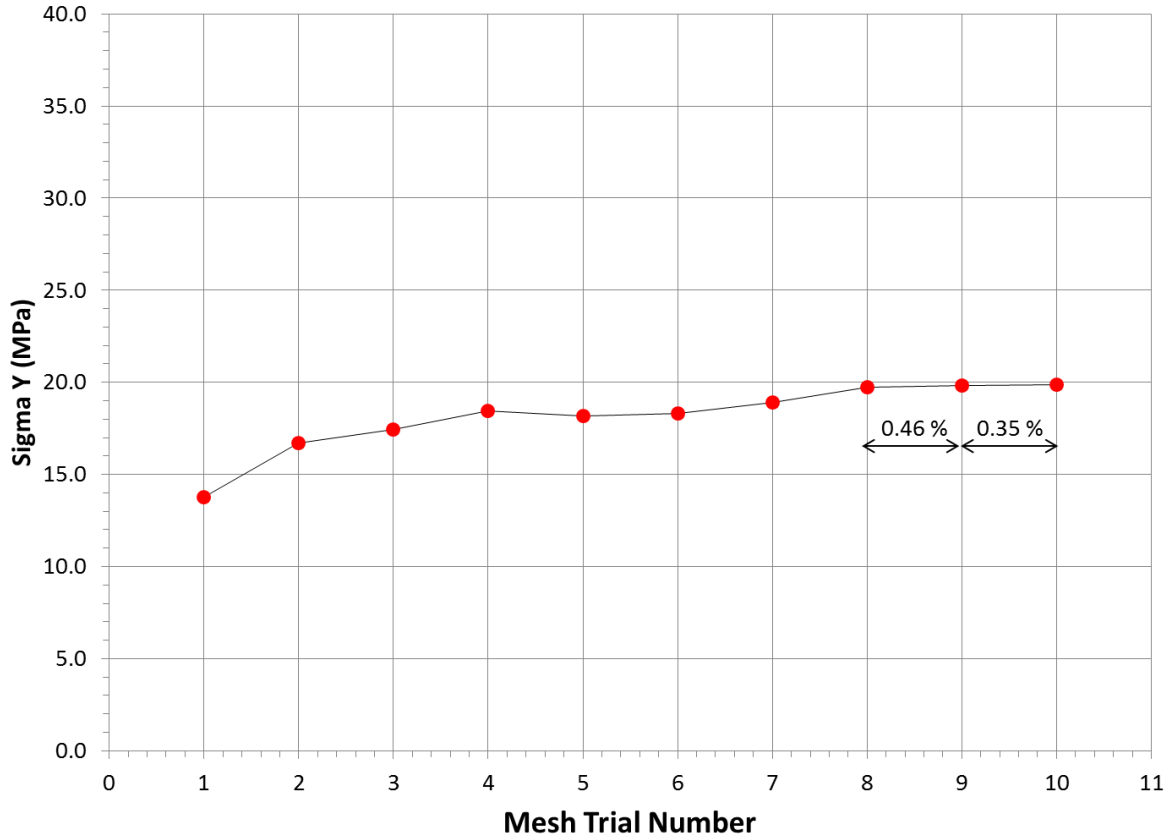


Figure 32. Mesh based solution convergence

In the above figure is a plot of y-directions stress as the mesh of the AFMF model is refined. When the difference between the new stress values associated with a new mesh was less than 0.5 percent, that mesh was used in the analysis.